CHARACTERIZATION OF MARINE STRATOCUMULUS CLOUDS AND AEROSOL-CLOUD INTERACTIONS DURING ORACLES

A THESIS SUBMITTED TO THE GRADUATE DIVISION OF THE UNIVERSITY OF HAWAIʻI AT MĀNOA IN PARTIAL FULFILLMENT OF THE REQUIREMENTS FOR THE DEGREE OF

MASTER OF SCIENCE

IN

ATMOSPHERIC SCIENCES

AUGUST 2018

BY

Ashley C. Heikkila

Thesis Committee:

Jennifer D. Small Griswold, Chairperson

Steven Howell

Alison D. Nugent

ACKNOWLEDGMENTS

First and foremost, I would like to thank my advisor, Jennifer Griswold for the coolest, most memorable experiences that I will forever remember and cherish. She gave me the greatest educational opportunities by allowing me to attend conferences in San Francisco, New Orleans, Austin, and all the way over to Manchester, England! Not only that, but she invited me to experience a major field campaign for two months in Africa! That was definitely an experience I will never forget! But aside from the traveling, Jennifer was the best advisor and teacher I could've ever asked for. I have learned more from her than any textbook I've ever read. Words cannot express the gratitude I feel for the invaluable knowledge and experiences I have received. Thank you for taking me under your wing in undergrad and allowing me to work with you through this advanced degree! You are the best!

I also owe many thanks to my committee, Steven Howell and Alison D. Nugent. Your patience and insight will help me achieve my advanced degree, and will give me fresh perspectives that will only serve to make this work better. Thank you in advance for your help and guidance!

Kayla and Jessie, you two were the best support system through this journey through grad school, and the best office mates in the world! Sanity is something hard to come by along this path, and I only managed to keep it because of both of you. Here's to new best friends for life. You guys rock.

Lastly, I owe my wife, Brittany, many thanks. We met before this all started, and you stuck by me through all the feels, and oh there were many! Thank you for all of the laundry and dishes. I owe you, probably for life. I love you so much. Thank you!

ABSTRACT

ORACLES (ObseRvations of Aerosols above CLouds and their intEractionS) is a 3-year field campaign taking place during the months of August, September, and October in the years 2017, 2016, and 2018, respectively, off the coasts of Namibia and São Tomé in the southeastern Atlantic (SEA). The purpose of this campaign is to study the effects of biomass burning aerosols (BBA) on climatologically important stratocumulus clouds. For this project, we focus on data collected during the 2016 field deployment and specifically focus on in-cloud data collected with the Flight Probe Dual Range - Phase Doppler Interferometer (FPDR-PDI) aboard the NASA P-3 aircraft. The FPDR-PDI has the ability to measure microphysical cloud properties such as instantaneous cloud drop size, cloud drop concentration, drop size distributions and liquid water content. In addition, we used black carbon (BC) measurements from the Single Particle Soot Photometer (SP2) to characterize aerosol and cloud properties during the flight.

We found that for the high BC level leg segments, cloud properties exhibited characteristics of the 1st Indirect Effect. The median diameter for all of the level legs combined was 14.6 μm. The median diameter was found to be 12.81 μm for the high BC cases, and 15.39 μm for the low BC cases, which indicates a shift of the size distribution to smaller droplet sizes with more "polluted" clouds and to larger droplet sizes for the "clean" clouds. The median effective radius for the high BC cloud legs was 9.02 μm and 11.43 μm for the low BC cloud legs. Overall, total number concentration (TNC) increased with BC, with the mean shifting downwards toward lower TNC with the low BC cases, and upwards towards higher TNC with the high BC cases.

TABLE OF CONTENTS

List of Tables

List of Figures

List of Abbreviations

ACI	Aerosol-Cloud Interactions
AOD	Aerosol Optical Depth
BBA	Biomass Burning Aerosol
BC	Black Carbon
CCN	Cloud Condensation Nuclei
CDNC	Cloud Drop Number Concentration
CDSD	Cloud Drop Size Distribution
FPDR-PDI	Flight Probe Dual Range – Phase Doppler Interferometer
LWC	Liquid Water Content
MBL	Marine Boundary Layer
MSc	Marine Stratocumulus Clouds
ORACLES	Observations of Aerosols Above Clouds and their Interactions
PDI	Flight Probe Dual Range – Phase Doppler Interferometer
RF	Routine Flights
SEA	South East Atlantic
SP2	Single Particle Soot Photometer
SSM	Seconds Since Midnight
TNC	Total Number Concentration
TOO	Target of Opportunity Flights

Chapter 1
Introduction

1.1 Marine Stratocumulus

On an annual mean, stratocumulus clouds cover approximately one-fifth of the Earth's surface making this cloud type the most dominant in regards to the area covered. It is estimated this cloud type covers 12% of the land surface and 23% of the ocean surface (Wood, 2012; Warren et al., 1986, 1988; Hahn and Warren 2007). Stratocumulus clouds that exist over ocean surfaces are referred to as marine stratocumulus (MSc), and will be the focus of this work. MSc are low, warm clouds that contain only liquid water, no ice, and generally exist below 2 km in the atmosphere in the marine boundary layer (MBL) region of the troposphere and can exist on a horizontal scale of ~1000km. The MBL is the lowest layer of the atmosphere that interacts with the surface of the ocean in a variety of ways relating to the vertical exchanges of momentum, mass, heat, and moisture between the surface and upper atmosphere (Houze, 2014). Focusing on the MBL where relative humidities are higher than over land, often greater than 75%, cloud cover is often more extensive, and presents as stratus and stratocumulus cloud layers (Wallace and Hobbs, 2006).

MSc are an important topic of study as they have the ability to reflect short-wave, solar radiation back to space acting as a cooling mechanism for the Earth. At the same time, but on a much smaller scale that creates a negative net radiative forcing effect, they absorb terrestrial, long-wave radiation from the Earth (Stephens and Greenwald, 1991; Hartmann et al., 1992; Wood, 2012). These cloud types are also susceptible to changes in aerosol amount that can alter the cloud lifetime, cloud coverage, and cloud albedo, which in turn have an additional impact on Earth's energy budget

(Sporre et al., 2014). MSc have been proven to produce the largest net radiative forcing on the global climate (Hartmann et al., 1992; Garay et al., 2008), but are poorly modeled in general circulation models (Garay et al., 2008).

MSc are typically found on the west coasts of continents (Houze, 2014) where upwelling of deep, cold ocean water replaces the warmer surface water. This upwelling of cold water results in a cooling of the moist air above the ocean's surface, which is the primary reason for the strong lower-tropospheric stability defined as the difference in potential temperature between 700mb and 1000mb (Wood, 2012). Easterly trades bring in warm air aloft equatorward over the western coasts that is held in place by strong subsidence from the subtropical high creating a strong capping inversion (Eastman et al., 2017; Wood, 2012; Garratt, 1990; Angevine et al., 2006). In these eastern oceanic subtropical locations, MSc exist 40-60% of the time based on an annual mean and are typically referred to as the semi-permanent subtropical MSc sheets (Wood, 2012). For this study, the MSc located off the west coast of southern Africa in the southeast Atlantic (SEA) will be highlighted. In this region of the Southern Hemisphere, these clouds exhibit a seasonality that is favored with a peak during the austral spring (September-November) when there is a more thermally stable lower troposphere (Painemal et al., 2014) that is intensified by the colder sea surface temperatures, and the enhancement of the inversion from the seasonal subtropical high pressure system that is fairly persistent (Muhlbauer et al., 2014). In addition to the seasonality, the thickness and coverage of MSc varies with the synoptic settings of the subtropical high, specifically with its strength (Klein et al., 1995; Klein, 1997; George and Wood, 2010; Toniazzo et al., 2011; Wood, 2012) and location (Klein et al. 1995; Garreaud et al., 2001; Wood, 2012). MSc formation and structure also depends greatly on the vertical structure of the MBL (Lilly, 1968; Albrecht et al., 1995b; Wood and Bretherton, 2004; Wood and Hartmann, 2006;

Bretherton et al., 2010b; Wood, 2012).

1.1.2 Marine Stratocumulus Formation and Maintenance

MSc formation can be understood with the help of Figure 1 borrowed from a review of stratocumulus clouds (Wood, 2012), which shows the key processes in the formation and maintenance of MSc. MSc typically form with large-scale cooling of the lower atmosphere resulting from emission of long-wave radiation to space during clear skies, which allows the upper boundary layer to reach saturation. Turbulent mixing is another mechanism by which the boundary layer may reach saturation. This often occurs from vertical shear of the horizontal wind (Garratt, 1992; Wood, 2012), or by buoyancy from the oceanic-atmospheric surface exchange caused by surface fluxes of energy and moisture (Wood, 2012). These two turbulent processes are denoted in Wood's figure by overturning grey arrows and upward pointing red and purple arrows, respectively. When the upper boundary layer reaches saturation, the trade inversion is not well defined due to weak turbulent eddies that reach differing heights. Once the saturation layer becomes thicker, the cloud top emits long-wave radiation (upward purple squiggly arrow), cooling the cloud layer and sea surface below (Paluch and Lenschow, 1991), which strengthens the inversion and helps to maintain the MSc (Wood, 2012).

Cloud-top radiative cooling can also act to thin cloud layers by inducing entrainment. Radiative cooling at cloud top creates convective instability, which causes convective circulations within the cloud (Lily, 1968; Wood, 2012). These convective circulations cause entrainment of dry air from just above the MSc-topped boundary layer into the moist cloud layer below, which causes evaporation of liquid droplets. Entrainment is then additionally enhanced by this evaporative cooling process, creating negatively buoyant air leading to a buoyancy reversal near cloud top. Thicker clouds also induce stronger entrainment through the production of buoyant turbulence from

increased cloud water; however, entrainment acts to thin the clouds, and thinning clouds decrease the rate of entrainment (Wood, 2012). These processes are termed the cloud-radiation-turbulent-entrainment feedback (Zhu et al., 2005, Wood, 2012) and leads to a strong negative feedback (Wood, 2012).

MSc are easily influenced by the atmospheric environment in which they form. Typically, marine environments are more pristine in regards to the particles in the atmosphere. When mainland particles, such as dust, smoke, and pollution are advected over the ocean, they have the ability to affect the microphysical properties of MSc, which is explained in Section 1.3. These particles are referred to as aerosol, and are described in detail below.

1.2 Aerosol

Aerosols are tiny particles that are suspended in the atmosphere, and can be either naturally occurring or anthropogenic. Some examples of naturally occurring aerosols are dust from deserts and volcanic ash from eruptions. Anthropogenic sources are human-induced pollutants such as smoke from intentional biomass burning and sulfates from burning coal and oil. Aerosols play a multi-faceted role in the atmosphere by interacting with solar radiation and influencing cloud formation and properties. They act as cloud condensation nuclei (CCN) during cloud formation by providing a platform for water vapor to condense upon. Clouds, having formed on aerosol serving as CCN, have the ability to either reflect or absorb solar radiation and emit infrared radiation depending on the type of cloud (liquid, ice, or mixed), the cloud thickness, and altitude in the atmosphere (Adams et al., 2012; Twomey, 1977). The amount of aerosols in the atmosphere can have an effect on cloud albedo, (Adams et al., 2012; Twomey, 1977), cloud lifetime, and precipitation (Adams et al., 2012; Albrecht, 1989). In addition, the type of aerosol and whether it is absorbing or reflecting influences these processes.

The outcomes of these interactions are dependent upon the aerosol type (absorbing, reflecting, or mixed), aerosol amount (high or low concentration), and where the aerosol is located with respect to the clouds (above, below, or mixed within the cloud layer (Huang et al., 2014).

1.2.1 Biomass Burning Aerosol

Specifically for this work, there is a focus on biomass burning aerosol (BBA) that is emitted as smoke into the atmosphere from agricultural clearing practices in south-central Africa. Each year, millions of square kilometers are burned in Africa on a seasonal basis (Giglio et al., 2006b; Roberts et al., 2009), causing it to be the number one source of biomass burning emissions from savannas (Andrae, 1991; van der Werf et al., 2003, 2006; Roberts et al., 2009). The biomass burning season in south-central Africa begins in May and typically ends in October, with July, August, and September being the most active fire months (Duncan et al., 2003). BBA from the fires are lofted into the mid-troposphere due to increased buoyancy from the heat of these fires, and are then advected equatorward over the SEA by the easterly trades where a semi-permanent MSc deck is located (Matichuk et al., 2007; Chand et al., 2009; Sakaeda et al., 2011). These BBA have significant effects on the radiation budget and microphysical properties of clouds, but the actual extent and to what degree are still not fully understood (Schulz et al., 2006; Ramanathan and Carmichael, 2008; Sakaeda et al., 2011).

1.3 Aerosol-Cloud Interactions

The physical processes of aerosol-cloud interactions (ACI) are fairly well-known, but their magnitudes still remain one of the largest uncertainties in climate models (IPCC, 2013). While the direct radiative effects of aerosols are an important aspect of the global climate, this paper

only addresses the 1st and 2nd indirect effects along with the semi-direct effect, which all focus on impacts to cloud properties, and are explained in detail below.

1.3.1 1st Indirect Effect

The 1st indirect effect is also known as the cloud albedo effect, or the Twomey effect, and is based on the work of Sean Twomey in his 1974 paper, "Pollution and the Planetary Albedo." The Twomey effect states that when clouds form in regions of higher aerosol loading, it produces clouds with more numerous smaller droplets, which increases the albedo of the cloud making it more reflective to incoming short-wave solar radiation (Twomey, 1974). This ACI acts as a cooling mechanism for the Earth, which is why any changes in cloud properties from changes in aerosol load can affect the global climate. The physical understanding of the cloud albedo effect is mostly well understood, but the magnitude of this effect is still widely debated (Lohmann and Feichter 2005; Wood, 2006), which is why climate models are not always in agreement on ACI.

1.3.2 2nd Indirect Effect

The 2nd indirect effect is also known as the cloud lifetime effect, or the Albrecht effect, and is based on the work of Bruce A. Albrecht from his 1989 paper, "Aerosols, Cloud Microphysics, and Fractional Cloudiness," and refers to the effect that a higher aerosol load has on the precipitation processes of a cloud. A cloud with numerous, smaller droplets will have a longer lifetime due to the lack of precipitation caused by the smaller droplets competing for available water vapor in the atmosphere (Albrecht, 1989). In addition to an increase in cloud lifetime, a suppression of precipitation may lead to an increase in the liquid water content (LWC), the height of the cloud, and the cloud coverage, but these are also susceptible to the meteorological conditions

at the time (Ackerman et al., 2004). Current understanding reveals that the reduction in cloud water sink from suppressed precipitation would lower the cloud base as the marine boundary layer cools, which would act to thicken the cloud (Albrecht, 1989; Wood, 2006), increasing the reflectance (Twomey, 1977; Wood, 2006). On the other hand, suppression of precipitation is known to reduce the stability of the atmosphere, which allows for more turbulence to occur in the MBL. An increase in turbulence increases the rate at which warm, dry air from above the MBL is entrained into the cloud, reducing the cloud thickness (Jiang et al., 2002; Ackerman, 2004; Wood, 2012). Global circulation models (GCMs) have a hard time modeling the 2nd Indirect Effect because these precipitation processes typically occur on a smaller scale that GCMs cannot resolve (Penner et al., 2006).

1.3.3 Semi-Direct Effect

The semi-direct effect, also known as the semi-direct aerosol effect on clouds, was coined by James Hansen in his 1997 paper, "Radiative Forcing and Climate Response." According to Hansen, dark-colored aerosol, such as soot, or absorbing aerosol, have the ability to absorb incoming solar radiation, which increases the local atmospheric temperature, and in turn decreases cloud cover by inhibiting the upward movement of moisture and reducing relative humidity (Hansen, 1997). The sign and magnitude of the semi-direct effect has the largest uncertainty of all the ACI's (Morgan et al., 2006; Sakaeda et al., 2011), but it is known that the vertical distribution of absorbing aerosols plays a role in the magnitude of the semi-direct effect. The impact of absorbing aerosols with the semi-direct effect can change with regards to the location relative to the boundary layer, and whether they are located above, below, or within (Johnson et al., 2004; Sakaeda et al., 2011) the cloud of interest.

The three ACI just described work together to modify the MSc deck creating complex interactions that are difficult to resolve. Continued research

into the complexities of these ACI is needed to fully understand the magnitude to which they affect climate regionally and globally.

1.4 Motivation

MSc have been a subject of interest for almost a century with the first research flights taking place in 1923 off the coast of California (Kloesel, 1992). Since that time, there have been numerous field campaign efforts to better understand these clouds, the influence of local aerosol on these cloud properties, and their overall impact on the global climate. In California, the most recent field campaign was the Marine Stratus/Stratocumulus Experiment (MASE and MASE II) that took place off the coast of Monterey in July 2005 and 2007, respectively. The focus for this mission was on the sub-cloud aerosol from ship tracks, above-cloud aerosol from fossil fuel combustion and biomass burning, and their influence on microphysical MSc properties (Lu et al., 2007, 2009).

The largest persistent MSc deck is located off the west coast of South America and was investigated during the VAMOS-Ocean-Cloud-Atmosphere-Land Study Regional Experiment (VOCALS-REX) in October and November of 2008. This field campaign focused not only on ACI and the microphysical properties of the MSc, but also on heat budgets and how they affect sea surface temperatures. In this region the majority of aerosol comes from biogenic pollution, industrial pollution, and biomass burning, which is similar to those aerosol found in California, but are predominantly confined to the coastal edge due to along-shore winds, whereas California typically experiences an offshore flow. The source of the industrial pollution comes from copper smelters and power plants that are situated on the west coast of South America (Wood et al., 2007).

The Southern African Regional Science Initiative (SAFARI 2000) was a field campaign focusing on southern Africa and the SEA that occurred in

August-September 1999, February-March 2000, and August-September 2000 that built on previous work from SAFARI-92 that focused primarily on land use cover and changes, biomass burning emissions, clouds and radiation, and hydrology meant to improve the political policies of environmental practices (Swap et al., 1999: SAFARI Science Plan).

Because ACI associated with MSc are still not fully understood, it is necessary to further try to quantify and understand these effects. The SEA provides a unique natural laboratory for these interactions as the aerosol type is mainly advected BBA with some dust from the Sahara Desert to the north on a lesser scale. Importantly, the climate-radiating MSc that exist in this region are integral to the energy budget, and are highly susceptible to anthropogenic aerosol effects. Distinctive from the SAFARI 2000 field experiment that also took place in and off the coast of south-central Africa, this work focuses specifically on the microphysical properties of the MSc in varying aerosol conditions, and include investigation into the effects on cloud droplet number distribution, total number concentration, median diameter, effective radius, and liquid water content that have the ability to affect radiation and climate.

Chapter 2
Mission Background and Data

2.1 ORACLES

ORACLES (ObseRvations of Aerosols above CLouds and their intEractionS) is a five-year NASA funded project with three one-month deployments to regions in the Southeast Atlantic (SEA) situated between 8N-22S and 20W-20E with the purpose of capturing the seasonality of aerosol-cloud interactions that occurs during the peak African biomass burning season of August, September, and October. These biomass burning aerosol (BBA) are lofted into the mid-troposphere and then transported westward over the SEA by the predominant easterly trade winds where they gradually settle over and into the MSc layer further from the coast. Figure 2 is a schematic of this concept, where the smoke is shown as a light brown haze. This region has some of the highest aerosol optical depths (AOD) in the world and can be seen via satellite situated above cloud layers, which increases AOD estimates by 25±6% globally. Satellites have proven that this region has a high AOD, but *in situ* data is needed to analyze the microphysical properties of the MSc that are highly susceptible to increases in aerosol concentration due to the fact that satellites have a difficult time retrieving cloud properties when there is aerosol present above cloud.

During the September 2016 deployment, there were thirteen science flights that consisted of Routine Flights (RF) and Target of Opportunity Flights (TOO) for a total of 101.1 flight hours. The flight paths can be seen in Figure 3 color-coded by flight date. The RF are shown as diagonal lines in Figure 3. They are shown as parallel lines in the figure for distinction, but in reality the flights were in the same location. These flights were designed to

gather mean states and variability of aerosol loads and cloud conditions for better comparison with climate models. These flights gathered data for the entire range of cloud and aerosol conditions, and not just for the highest or lowest conditions. The TOO (variable lines in Figure 3) addressed the previously mentioned specific conditions of interest and are highly dependent on the forecasted meteorological conditions from the previous day. These flights were meant to address the specific aerosol-cloud-radiation interaction objectives of ORACLES.

2.2 Instrumentation and Data

2.2.1 FPDR-PDI

Data from the FPDR-PDI (Flight Probe Dual Range – Phase Doppler Interferometer) was collected to analyze cloud microphysical properties. The PDI, which I will refer to from now on, instantaneously and non-intrusively measures cloud droplet size (1-1000 μm), cloud droplet velocity, and cloud droplet arrival time using an advanced laser-based technique. Figure 4 from Chuang et al. (2008) shows the initial laser beam is split into two beams of equal intensity by a beamsplitter. These two beams then pass through the front focal lens where they are focused to an intersection point. This intersection is where the droplets are detected and is referred to as the probe volume. The probe volume scatters the light as cloud droplets pass through, and the scattered light is then collected by an optical receiver lens and an aperture that transfers the signal to three photodetectors. The signal from the photodetectors is sent to a processor, which gives droplet size and velocity. These detected Doppler bursts have both a Gaussian envelope and a fringe pattern, and the droplet size is the phase difference of the burst between detectors. In addition to instantaneous products, there are a number of derived products that will be used for this work. These products are cloud drop number concentration (CDNC) up to 100,000/cc, total number

concentration (TNC) effective radius, median diameter, liquid water content (LWC), and spectral width.

CDNC (dN/dlogDp/cc) as a function of droplet diameter (μm) gives the size distribution of cloud droplets for each pass through a cloud using the PDI. The droplet size distribution offers a broad glimpse of the microphysical aspect of a cloud. Narrow size distributions indicate a more homogenous cloud than a cloud with a broader size distribution. Autoconversion favors broader size spectrums as larger droplets collide and coalesce with smaller cloud droplets (Young, 1993; Hudson et al., 1997). Additionally, where the peak in the size distribution occurs is important. A peak towards the lower end of the size spectrum could be indicative of a cloud that formed in a region with a higher aerosol load and might indicate a more polluted region, whereas a peak towards the larger end of the size distribution may indicate a "clean" cloud that formed in a more pristine environment.

TNC is given in #/cc, and is distinct from CDNC in that it is independent of droplet size. The total number of droplets in a given volume of air is a useful product for investigating the trend in microphysical properties as a function of the TNC.

Effective radius (μm) is defined as the ratio of the 3rd moment to the 2nd moment of the size distribution and is an important parameter as it is easily compared to remote sensing data as many satellites offer this product. It is a radiative measure of the size distribution (Wallace and Hobbs, 2006). The equation is as follows: $\int_0^\infty r^3\, n(r)dr \,/ \int_0^\infty r^2 n(r)dr$, where $n(r)$ is the number concentration of cloud droplets with radius r (Reid et al., 1999).

The median diameter (μm) is the peak in the size distribution where 50% of the droplets are larger and 50% are smaller. It is a useful parameter when looking at drop size distributions. A shift in median diameter, or peak of the size distribution, to larger or smaller droplets could be due to clouds forming in more clean or polluted conditions, respectively.

LWC is the mass of liquid water per unit volume of dry air and is often expressed in g/m^3. It depends heavily on the dynamics of the atmosphere. LWC in MSc can be useful in determining if the cloud can produce precipitation, or drizzle in the case of MSc, as clouds generally need a LWC of at least 0.5 g/m^3 for this to occur (Cotton and Anthes, 1989).

Distribution width, as defined in this work, is the difference between the 90^{th} percentile and the 10^{th} percentile of the number distribution (counts per size bin). Distribution width is useful for observing spectral broadening toward larger droplet sizes, which is an indicator of the potential for clouds to precipitate.

2.2.2 SP2

Data from the SP2 (Single Particle Soot Photometer, Droplet Measurement Technologies) was used to categorize "clean" vs "polluted" clouds and to compare the microphysical cloud properties in each of these categories. The SP2 uses laser beams at 1064 nm to heat light-absorbing refractory BC particles to vaporization. These BC particles, when heated, emit incandescent light when vaporizing. The SP2 detects BC particles between 70 and 700 nm (Schwartz et al., 2006).

BC, also referred to as soot, are particles that typically result from incomplete combustion of fossil fuels, biofuels, and biomass. BC not only acts as CCN for cloud formation, but it is a strong absorber of solar radiation. It can act to warm the atmospheric environment creating cloud burn-off as per the semi-direct effect (Liu et al., 2014) discussed in Section 1.3.3.

Chapter 3
Methods

3.1 Level Leg Analysis

For each science flight, in-cloud, level legs were used to gather the mean values of cloud properties. For this work, level leg segments include ascent out of or descent into the cloud. To accomplish this, CDNC and pressure altitude as a function of time in seconds since midnight (SSM) was plotted to find where there was cloud data, which is shown as the rainbow colors in Figure 5. The pink line is the pressure altitude, and tells us where in the atmosphere the plane was flying. These "rainbow plots" are an example of how the timing of the level legs was determined. Figure 6 shows the same rainbow plot as in Figure 5, but is zoomed in on the start and end times of L2 as denoted by the black arrows. The level legs are circled in black and labeled as L1, L2, and L3. These times were then used to average the various cloud properties described in Chapter 2. On average, each level leg was near 8 minutes long. Statistically, longer cloud legs would be more beneficial, but with a shared research mission, it is not always possible.

3.2 BC Sorted Data

To observe the differences in microphysical cloud properties between in-cloud, level legs, each leg was classified according to high BC values of greater than 30 $\mu g/m^3$ and low BC values of less than 2 $\mu g/m^3$. The BC values presented here have been averaged over each individual level leg. High BC legs are an indication there is more BBA present and interacting with these clouds. Low BC values are an indication that these clouds may have formed in a more pristine environment assuming LWC has remained relatively

constant. Because BC is just one type of BBA, it may not be entirely representative of the total aerosol count in-cloud, but for the purpose of this work, it is the best variable for in-cloud presence of BBA as it is not susceptible to droplet shatter in the aerosol inlet, which can alter particle counts.

3.3 Location Analysis – Plotting by Latitude and Longitude

The latitude and longitude for the level legs is important to note when comparing the cloud microphysical properties as the location with respect to the coast of western Africa could have an impact on these different properties. The locations closest to and furthest from the coast most likely have less BBA aerosol impacts than those locations near the middle of the flight paths. This idea is displayed in Figure 2, where the plume directly off the coast is suspended at a higher altitude than the cloud layer, and begins to sink into the cloud layers as it travels westward. In addition, there is a spatial variation in cloud properties. Figure 7 shows the BBA plume as warm red colors, and indicates that it is being advected westward over the SEA and mixing with the MSc (inlet figure). The BBA plume is greatest from the Equator to ~18S and 8W to the coast.

For cases of high and low threshold BC, these cloud legs will be plotted by their location for further analysis in Section 4.4.

3.4 Average Altitude of Level Leg in Cloud

The average altitude for each level leg was calculated and sorted into four altitude categories: 0-450, 450-600, 600-750, 750-900, and 900-1100 m, which can be seen in Table 1. The altitude at which clouds are located in the atmosphere can affect cloud microphysical properties. It is known that in clean clouds, effective radius increases with decreasing temperatures (with

height above cloud base). Effective radius, however, remains relatively constant throughout polluted clouds (Rosenfeld et al., 1999). In MSc, LWC increases with height in a cloud along with the median diameter. For marine clouds that are “clean” the droplet number does not tend to change with height, but for “polluted” clouds, droplet number concentration tends to increase with height (Miles et al., 2000).

Chapter 4
Results

4.1 Level Leg Average Cloud Characteristics

For 2016, there were thirteen attempted science flights, one of which ended within the first two hours of taking off due to a mechanical malfunction of the aircraft, resulting in twelve full science flights. Of those twelve science flights, eleven of them included in-cloud level legs. In addition to the science flights, there is a transit flight to Ascension Island that was noteworthy as it was able to capture the progression of the plume, the horizontal expanse of the MSc cloud deck, and also the out-of plume pristine maritime atmosphere. In total, with the transit and science flights, there were twelve flights that had thirty-two in-cloud level leg segments.

September 10, and 27, 2016 each had one in-cloud level leg segment that was broken up into two separate legs L1a, and L1b to compare the differences of the broken cloud segment. Flight paths from 2016 can be seen in Figure 3, and are color coded by flight date. The longest level leg was 993 seconds and the shortest leg was 148 seconds long. On average, the level legs were 485 ± 194 seconds long. With the average flight speed of 130 m/s, we were able to cover approximately 63 ± 25 km of cloud on a horizontal scale per level leg. The cloud properties along with other key parameters measured during each level leg can be found in Table 1.

4.1.1 Cloud Drop Size Distributions

Figure 8 shows CDNC as a function of cloud drop diameter for each level cloud leg giving the cloud drop size distributions. Each flight is color coded by date, with the overall mean in black. There is a jump in data shortly after 100 μm, which is an artifact of a processing error and will need to be

removed in the future, but it does not affect the results found in this work. The median diameter of the overall mean drop size distribution is 14.6 μm. In comparison to the individual cloud legs, the mean has a broad distribution spectrum as expected due to the varying microphysical properties of each cloud leg, which is highly dependent upon the latitude and longitude of the cloud legs and the proximity of BBA with respect to the cloud. There are two flight days that stand out when looking at the overall size distributions. The first is 9-27-2016, shown in magenta, which was the first leg of the transit flight returning to Wallops, VA. This flight from Walvis Bay, Namibia to Ascension Island has some of the lowest BC concentrations and largest droplet diameters. Specifically, the leg L1b had the largest median diameter of 24.6 μm with a low BC concentration of 1.7 $\mu g/m^3$. L2 on 9-20-2016 shown in light purple has the lowest median diameter of all the flight legs at 5.6 μm with a high BC concentration of 95.8 $\mu g/m^3$. These are indicative of the 1st Indirect Effect where we would expect larger median diameters with lower concentrations of aerosol and smaller median diameters with higher concentrations of aerosol.

4.1.2 Median Diameter vs. TNC

For all level legs, the median diameter is shown as a function of TNC with each flight having color-coded shapes in Figure 9 that correspond to the flight dates listed with the color bar. The RF are shown as squares, the TOO are show as circles, and the Transit is shown as triangles. Most of the flights are clustered around the trend line shown in red. By looking at the figure, it would appear that the trend line is decreasing with a value of -0.005, suggesting that median diameter is decreasing with increasing TNC. After doubling the error estimate of the slope which gives a value of .013, it can be determined, then, that it is not significantly different from zero. Per the 1st Indirect Effect, as the TNC increases, the median diameter should be

decreasing as more droplets must compete for the available water vapor, which results in smaller droplets.

The magenta squares show the level legs from 9-27-2016, and deviate far from the trend line. The large median diameters and low TNC indicate this flight may be in extremely pristine atmospheric conditions out of reach of the BBA plume as the aircraft heads toward Ascension Island. Another outlier is the flight on 9-24-2016 shown in light purple, specifically with legs L2 and L3. The median diameters were some of the smallest at 5.6 and 8.1 μm with also the lowest TNC at 77.36 and 120.87/cc, respectively. After checking the LWC with L2 at 0.015 and L3 at 0.058 g/m^3, these very low LWC values are most likely the reason for the anomaly. Legs L1a and L1b on 9-10-2016, shown in yellow, also had low median diameters with low TNC deviating far away from the trend line, and in both of these legs, there were also extremely low LWC calculations of 0.116 and 0.096 g/m^3, respectively.

4.1.3 Effective Radius vs. TNC

Figure 10 shows effective radius as a function of TNC and is color-coded in the same manner as Figure 9. Similar to Figure 9 described above, we would expect a decrease in effective radius with an increase in TNC as per the 1st Indirect Effect. The trend line follows our expectations and effective radius decreases with an increase in TNC, and many of the level legs cluster around this trend line with an R^2 value of 0.131. Doubling the error estimate of the slope gives a value of .0097. This number is smaller than the slope value of -.0104, which means that this decreasing trend line is statistically significant. The same cloud legs as in Figure 9 are the same outliers in this figure, as are the speculations, and were shown to be located on the edge of the climatological plume from Figure 7, and possibly may have formed in a cleaner environment.

4.1.4 TNC vs. BC

TNC as a function of BC as shown in Figure 11 has a positive trend line indicating that as BC increases, so follows the TNC, which we would expect from the 1st Indirect Effect that if there are more aerosol particles available for condensation, there will be more numerous, smaller cloud droplets. However, doubling the error estimate of the slope gives a value of 1.15, with is much larger than the actual slope value of 0.387, which shows that it does not have statistical significance. In addition, many of the level legs, are far from the trend line with few clustered around it. It can be noted that initially with low BC, the TNC increases, but after 90 $\mu g/m^3$, the TNC becomes less again. Because BC is a strong absorber of sunlight, this could be related to the Semi-Direct Effect where cloud burn-off is evaporating cloud droplets. This is seen on 9-24-2016 shown as light purple circles that had larger concentrations of BC and lower TNC values.

4.1.5 Median Diameter vs. BC

Median diameter as a function of BC is shown in Figure 12. There is a downward trend line, and when doubling the error estimate of the slope it gives a value of 0.038, which is smaller than the value of the slope at 0.046, which means it is statistically significant. Similar to Figure 9 with median diameter as a function of TNC, where we expected to see smaller median diameters with increasing TNC, we expect and see smaller median diameters with increasing BC values, which corresponds to the 1st Indirect Effect.

4.1.6 Effective Radius vs. BC

Effective radius as a function of BC is shown in Figure 13. The trend line indicates decreasing effective radii with increasing BC, which is evidence of the 1st Indirect Effect. The double of the error estimate is 0.03, which is less than the slope value of 0.041 meaning it is statistically significant. This

is similar to Figure 10 as we would expect smaller radii with higher concentrations of aerosol, meaning the cloud would be more reflective with smaller droplets.

4.1.7 Liquid Water Content vs. BC

LWC as a function of BC is displayed in Figure 14. The red line denotes the linear trend where LWC is showing an overall decrease with an increase in BC. However, twice the error estimate of the slope is 0.0037, which is larger than the slope value of 0.0031, which is not statistically significant. Similar to Figure 11, there is an increase in LWC with increasing BC, and then a decrease in LWC with BC with the largest BC concentrations. The Semi-Direct Effect is a possible explanation for the reduction in LWC. Level leg L1a from 9-27-216 has the highest LWC at 2.153 g/m^3, with the majority of the legs below 1 g/m^3. Overall, legs L1a and L1b on 9-10-2016 and legs L2 and L3 on 9-24-2016 had the lowest LWC of all the science flights with values of 0.116, 0.096, 0.0125, and 0.0578 g/m^3, and BC values of 1.99, 1.49, 95.8, and 136.7 μg/m^3 respectively. As per the 2nd Indirect Effect, the cloud lifetime would increase with increasing aerosl, which might suggest that LWC would also increase as the cloud would not precipitate out, however, this is usually the case during the night and early morning, and is seen less in the afternoon. Radiative cooling at cloud top creating convective circulations may have caused entrainment and evaporation of cloud drops also reducing the LWC of a cloud (Caldwell and Bretherton, 2009).

4.2 BC Sorted Level Leg Data

The data presented in section 4.1 consists of all the level legs together in one plot for each key variable to show the mean overall results. Below in section 4.2, we have sorted the key variables into cases of high BC (> 30 μg/m^3) and low BC (< 2 μg/m^3) to focus on the microphysical differences of

these MSc as a function of varying BC concentrations. For figures in sections 4.2.2 to 4.2.5 the x-axes are different BC values according to the thresholds. The high BC x-axis ranges from 30-180 μg/m^3, and the low BC x-axis spans from 0-2.4 μg/m^3. The y-axis will remain the same for each key variable between the two cases.

The BC values for all level legs can be found in Table 1. For each of the high and low threshold cases, there are 10 legs. The highest BC value for the level legs was found to be 136.7 μg/m^3, which occurred during L3 on 9-24-2016. The lowest BC value found for a level leg was 1.03μg/m^3 and occurred during L2 on 9-10-2016.

4.2.1 High vs. Low BC CDSD

Separating the distributions into high BC values and low BC values gives a clearer picture of the effects these BBA may have on the size distributions and median diameter. Figure 15 shows CDNC as a function of cloud drop diameter with the high BC threshold in the top panel and the low BC threshold in the bottom panel. Again, the flights are color coded in the same respect as Figure 8, and the false data exists as well and will be removed in the future. The median diameter for the high BC threshold was found to be 12.81 μm, whereas the median diameter for the low BC threshold was larger at 15.39 μm. This highlights a shift in the peak size distribution from the total size distribution as seen in Figure 8 with a median diameter of 14.6 μm, to the smaller sizes for high BC and the larger sizes for low BC, as denoted by the pink dotted line, and is described in section 2.2.1. This is what we expect to see in validation for the 1st Indirect Effect as detailed in section 1.5.1.

4.2.2 High vs. Low BC Median Diameter

Figure 16 shows median diameter in microns as a function of the high BC threshold of greater than 30 μg/m^3, while Figure 17 shows the median diameter as a function of the low BC threshold of less than 2 μg/m^3. Each level leg is color-coded to the flight date listed beside the color bar with RF shown as squares, TOO shown as circles, and Transit shown as triangles. As noted above in section 4.2.1, the median diameter of the high BC threshold was found to be 12.81 μm, whereas the median diameter of the low BC threshold was larger at 15.39 μm. In both cases, the trend line is decreasing showing a relationship to the 1st Indirect Effect, but was found to be statistically insignificant for the both the low and high BC cases. When doubling the error estimate, both values were larger than the slopes.

The largest median diameter for the lower BC cases was found to be 24.8 μm for L1b on 9-27-2016, and the smallest median diameter was 9.4 μm for L1b on 9-10-2016. Comparing the higher BC cases, the largest median diameter was found to be 16.8 μm for L3 on 9-6-2016 and the smallest median diameter was found to be 5.6 μm for L2 on 9-24-2016. Overall, the high BC cases had the lower median diameters, which is what we would expect from the 1st Indirect Effect.

4.2.3 High vs. Low BC TNC

Figure 18 shows TNC as a function of the high BC threshold, whereas Figure 19 shows TNC as a function of the low BC threshold whose values are mentioned in section 4.2. In both the high and low BC cases, the trend line is decreasing, which would indicate that when BC increases, so does the total concentration of cloud droplets. They were both found to be statistically significant as the doubling of the error estimates was smaller than the slope value. This is not what we would expect with the 1st Indirect Effect, but because of the strong absorption of BC to sunlight, the higher BC cases may

be indicating that the Semi-Direct Effect is occurring. For the low BC cases, the trend line may not be representative of what is actually occurring as BC is not the only aerosol that may be present, it is just what we are able to detect in-cloud for the 2016 deployment. The R^2 value was found to be 0.479 for the high BC cases, and 0.378 for the low BC cases, which are both strong relationships. One thing to note is the mean trend line has shifted downwards in the low BC cases in Figure 19 from the high cases from Figure 18. The median value for the low BC cases was found to be 181/cc and 297/cc in the high BC cases. This is what we would expect to see per the 1st Indirect Effect that higher concentrations of aerosol lead to more numerous cloud droplets.

4.2.4 High vs. Low BC Effective Radius

Figure 20 shows effective radius as a function of the high BC threshold, and Figure 21 shows effective radius as a function of the low BC threshold. For both cases, the trend line is decreasing indicating that as BC increases, the effective radius decreases, which is what we would expect per the 1st Indirect Effect. However, they were both found to be statistically insignificant as the doubling of the error estimates was larger than the slope value. Both figures show a very low R^2 value with the high BC case having a value of 0.073, and the low cases having a value of 0.016. Overall though, there is a clustering around the trend line in both high and low BC cases. The median effective radius is 9.02 μm and 11.43 μm for the high BC and low BC cases, respectively. This indicates that the effective radii are smaller with the high BC concentrations, and larger with the low BC concentrations, which is what we would expect to see.

4.2.5 High vs. Low BC Distribution Width

In Figure 22 and Figure 23, the 10^{th}, 50^{th}, and 90^{th} percentiles of the drop size distribution are shown as blue, pink, and green lines, respectively. For both of the figures, the y-axis displays the droplet size diameter in microns and the x-axis gives the time of flight in local Namibian time. Figure 22 shows L4 on 9-24-2016, and Figure 23 shows L4 on 9-14-2016, which are some of the highest BC (126.7 $\mu g/m^3$) and the lowest BC (1.16 $\mu g/m^3$) cases, respectively. The first thing to note is that the lower BC case has larger droplet diameters overall, and is very uniform throughout the cloud leg. Figure 22 is very interesting because it starts out with small droplet diameters, and then has an abrupt increase towards larger diameters and a wider distribution. The wider distribution between D10 and D90 is indicative of spectral broadening towards larger droplet sizes, which is suggestive of a cloud that is capable of precipitating with droplet diameters upwards of 30 μm as shown in green.

4.2.6 High vs. Low BC LWC

Figures 24 and 25 show LWC as a function of high BC cases and low BC cases, respectively. For both cases, the trend line is decreasing, which might suggest that an increase in BC leads to an decrease in LWC, which is not was is expected from the 2^{nd} Indirect Effect. We would expect that LWC would increase with increasing aerosol, which would lead to a longer cloud lifetime allowing the cloud to become thicker with more liquid water. For the high BC cases, as with TNC, the Semi-Direct effect may be occurring as the solar absorbing BC would act to induce evaporation and cloud burn-off. The average LWC for the low BC cases is 0.63 g/m^3 and the average for the high BC cases is 0.56 g/m^3. A study by Thompson et al., 2007 claimed that the average LWC for MSc clouds was 0.45 g/m^3. While our measurements are

slightly above this previous finding, it is not far off. We found that the low BC cases were not statistically significant, but the high BC cases were.

4.3 Latitude and Longitude Effects

Each of the variables listed in this section have been individually mapped according to the latitude and longitude of the flight paths for each level leg. Each level leg is color-coded by flight date. The high BC legs are shown as large asterisks, and the low BC legs are shown as large hexagons and follow the values on the color bar. Each second of flight time was plotted for each variable for the time spent in level cloud legs. There is variability within each cloud leg along with the location of each leg. We expect BC to vary spatially from north to south and east to west as can be seen by Figure 7 that shows the climatological BBA plume. The RF flights of 8-31-2016, 9-10-2016, and 9-25-2016 have been offset to show the separate level legs, but in reality, the flight paths were flown on nearly the exact same path.

4.3.1 BC Variability

The variability of BC and the location of these level legs are shown in Figure 26. The range of BC values is from 0.4 to 208 $\mu g/m^3$. The higher BC legs are predominantly situated to the north above 15S, particularly in the region along the coast between 8 and 11 E as can be seen along the flight paths from 9-6-2014 and 9-24-2016 denoted as green and red colors. This is exactly where the BBA plume is supposed to be more concentrated according to Figure 7. What is interesting to note is that for the RFs the concentration of BC varied by day. On 8-31-2016 shown as the red line, there were higher concentrations of BC shown as green and light blue, and lower concentrations of BC shown as dark purple for the other two RFs. Also, 8-31-2016 is showing a gradient of BC along the flight path with the higher concentrations of BC occurring in the middle of the flight path shown in the light green. L1b on 9-

27-2016, shown on the dark purple line, also has some of the lowest BC concentrations, and by referring back to Figure 7, this leg was furthest from the climatological smoke plume.

One thing to mention here is that 9-24-2016 was an extremely variable research flight in terms of the data. Looking back to Figure 22, which shows the distribution widths for L4 on 9-24-2016, and then looking at Figure 26 for the flight path on 9-24-2016, L4 is the southernmost cloud leg on that path shown in light purple. L4 begins as a heavily polluted cloud as denoted by the bright red coloring in Figure 26, and then transitions to a dark blue color, which indicates it is most likely less polluted. Figure 22 shows a cloud with smaller droplets that then jumps to a cloud with larger droplets. This signifies the transition from a polluted to a clean environment and is indicative of the 1st Indirect Effect.

4.3.2 Median Diameter Variability

The variability of median diameter and the location of these level legs are shown in Figure 27. The median diameter values for the color bar range from 3 to 35 μm. L1b on 9-27-2016 has one of the largest ranges of median diameter from 3-35 μm. Some of the smallest median diameters were located right along the coast as can be seen by looking at the flight path on 9-24-2016. These level legs also had some of the highest BC values that can be seen in Figure 26. Many of the level legs had similar median diameters between 13-16 μm as can be seen by the bright green colors. The largest median diameters were found on 9-6-2016 in the northern most cloud leg. Looking back at Figure 26, there was a gradient in this cloud leg with low concentrations in the northern part of the leg transitioning to greater concentrations moving south. This gradient might account for the anomaly of large median diameters in a leg with higher BC concentrations. Being this was the transit flight that flew furthest from the plume we would expect a shift towards larger droplets, which we do see. Also, the transit flight on 9-

27-2016 had large median diameters denoted by the greens and reds. As from the previous Figure 26, these had very low BC concentrations, and flew furthest from the plume in what we would expect to be a more pristine marine environment. We also see that it is quite variable as expected as there is more water vapor available for a smaller number of droplets allowing some to grow to larger sizes.

4.3.3 Effective Radius Variability

The variability of effective radius and the location of these level legs are shown in Figure 28. The range of effective radii on the color bar is from 1.6 to 39 μm. Similar to median diameter in Figure 27, the smallest effective radii are located in the northern most legs on the 9-24-2016 flight path, which is where the largest concentrations of BC were located. The legs along the routine flights (diagonal offset lines) seem to have a larger effective radius, especially the 9-10-2016 flight path, which is also where the smallest concentrations of BC were located. Like the BC map, the RFs varied and 8-31-2016 had larger effective radii than the others. This is consistent with the findings in the southeast Pacific where the largest effective radii were found offshore removed from the majority of the pollution (Bretherton et al., 2010).

4.3.4 TNC Variability

Figure 29 shows the variability of TNC and the exact location of these legs on the flight paths. The TNC concentrations on the color bar ranged from 0.2 to 808/cc. While the low BC legs along the RFs show low concentrations of TNC, shown as blue colors, as would be expected, the low BC legs found along the TOO flight of 9-14-2016, show higher concentrations of TNC as can be seen by the green hexagons. It could be that this region had low BC concentrations, but higher concentrations of organic aerosol, but BC is the only variable we were able to detect in-cloud for the 2016 deployment. The

RF on 8-31-2016 had the highest concentrations as shown by the red asterisks, and like the BC map in Figure 26, there was a gradient along this flight path and the legs differed by each day.

4.3.5 LWC Variability

Figure 30 shows LWC for each level cloud leg. The values in the color bar range from 0.01 to 2.7 g/m^3. LWC is extremely variable throughout each of the cloud legs and also in regards to the location. The flights with the highest BC, such as the northernmost legs on flight path 9-24-2016, have the lowest values of LWC, which could be a strong indication of the semi-direct effect. This conclusion comes from the fact that it does not follow what we would expect with the 2nd Indirect Effect. We would expect that as the smaller droplets suppress precipitation, the cloud would have the opportunity to become thicker as cloud water would not be precipitating out. It could also be that the clouds were experiencing high levels of entrainment, which would act to thin the cloud and reduce the LWC.

4.4 Altitude Effects

Table 1 has BC, median diameter, effective radius, LWC, and TNC sorted by altitude in feet and also meters as mentioned in Section 3.5. BC concentrations are varied throughout the differing altitudes, but the majority of the high threshold BC are located in the 900-1100 m altitude. The largest median diameters at ~24 are found in the 750-900 m range, but this altitude range also has ~11 μm median diameter sizes. In addition, the second largest median diameter at ~20 μm is found in the 0-450 m altitude range along with the smallest median diameter at ~5 μm. For the effective radius, similar to the median diameter, the largest effective radii are found in the 750-900 m range, but are still variable throughout the rest of the altitude classifications. The largest LWC values are also found in this 750-900m range, but again,

the LWC values are variable throughout the altitude levels. Lastly, the largest TNC concentrations of ~500/cc are found in this 750-900 m altitude classification, but the second largest of ~ 400/cc are found in the 0-450 m range along with some of the lowest vales at ~77/cc. The highest variables are found in both the 0-450 and 750-900 m ranges. The largest values of the cloud microphysical properties are found in the 750-900 range. LWC and cloud droplet size are known to increase with height above cloud base until reaching cloud top where entrainment occurs.

Chapter 5
Conclusions and Discussion

5.1 Summary

An investigation of the microphysical MSc properties in varying CCN and OA environments was conducted for the ORACLES 2016 deployment to Walvis Bay, Namibia using flight data from the PDI and the SP2 instruments onboard the NASA P-3 Orion aircraft. Of the twelve successful science flights, eleven of the flights carried out in-cloud level leg maneuvers. An additional transit flight to Ascension Island on 9-27-2016 was included in the analysis, and contained one level leg maneuver for a total of 32 level leg segments during ORACLES 2016. To analyze these cloud properties, the level legs were sorted in numerous ways: by BC concentration thresholds of greater than 30 $\mu g/m^3$ and less than 2 $\mu g/m^3$, by latitude and longitude, and by average cloud altitude. Because aerosol effects on clouds are still not fully understood, and because the SEA region has not been fully investigated, this study set out to create a preliminary analysis of how MSc in this region react to an atmospheric environment composed primarily of BBA from fires from the mainland. The following is a summary of our results:

- The median diameter of the all-inclusive CDSD was found to be 14.6 μm. The CDSD peak shifted to the left towards smaller droplet sizes with the higher BC level legs and had a median diameter of 12.81 μm. It shifted to the right towards larger droplet sizes with the low BC level legs and the median diameter was found to be 15.39 μm. This is evidence of the 1st Indirect Effect where clouds exposed to higher

concentrations of aerosol tend to form smaller, more numerous cloud droplets.

- The effective radius results also indicate that the clouds with high BC had smaller cloud droplets as the median effective radius was found to be 9.02 μm. The low BC level legs had a larger effective radius of 11.43 μm. The difference is not as large as with the median diameter, but is still evidence of the 1st Indirect Effect.

- Overall, TNC was found to increase with an increase in BC, but the lowest and highest legs when separated decreased with increasing BC. This could be attributed to the Semi-Direct Effect as BC is highly absorbent of solar radiation, which would cause cloud-burnoff. The average TNC for the high BC cases was found to be 297/cc and for the low cases, we calculated an average of 181/cc. Per the 1st Indirect Effect, clouds that form with higher concentrations of aerosol, have more numerous cloud droplets that are smaller as they compete for the available water vapor, when LWC remains constant.

- Overall, LWC was found to decrease with an increase in BC. This is not what we would expect with the 2nd Indirect Effect. As BC increases, it should prolong the lifetime of the cloud and inhibit precipitation, allowing the cloud to grow thicker and increase in LWC. As discussed in Section 4.1.7, this may not always be the case due to entrainment and burn-off from the Semi-Direct Effect.

- High and low level legs of BC, median diameter, effective radius, TNC, and LWC were plotted as a function of their latitude and longitude. Cloud properties to the north exhibited the strongest Indirect Effects relationships, especially with the TOO flights of 9-24-2014 and 9-6-

2016, that went up along the coast. This is where the BBA plume was at the highest concentration and most likely had an effect on the cloud microphysical properties. The RF flights exhibited variability from day to day, even though they flew along the same path. This shows that the BBA plume itself is variable, and not always constant The transit flight on 9-27-2016 was furthest from the coast and exhibited "clean" cloud properties.

- After separating the cloud properties according to their altitude, it can be seen that the highest values of LWC, median diameter, effective radius, and TNC were found between 0-450 m and 750-900 m. BC was variable throughout, but the largest concentrations were found in the highest altitude group of 900-1100 m.

This was a first look into the microphysical cloud properties that are affected by BBA from the ORACLES 2016 deployment. The data exhibited evidence for the 1st Indirect Effect with smaller (larger) cloud droplets for higher (lower) aerosol concentrations. And overall, there was a greater (lesser) number of droplets with higher (lower) BC values, which is also evidence for the 1st Indirect Effect.

Evidence for the 2nd Indirect Effect was not found in this work. We would have expected increasing LWC with an increase in aerosol, but the opposite was found. This may be due to the comparison with BC. BC is highly absorbent of solar radiation, which can easily cause cloud-burn off with the Semi-Direct Effect.

Studying these MSc is important for knowledge of the complexities of ACIs and how they may affect the climate now and in the future, especially in regards to global climate models. Much of the errors associated with climate models come from a lack of understanding of these complex processes. While this work did not solve that problem, it gave an idea of not only how difficult

it is to pinpoint the exact processes at work, but that these clouds are absolutely being affected by increased aerosol loads, and need more attention.

5.2 Issues

While completing this analysis, there were several issues that need to be addressed for future work. Because BC is just one type of aerosol from BBA, there might be more or less organic aerosol present that could be affecting the cloud properties, but we could not properly measure them in-cloud for the 2016 deployment as there was no counter virtual impactor (CVI) inlet, which would allow us to quantitatively use in-cloud CCN and aerosol measurements, by avoiding the issue of shatter. The CVI inlet separates cloud droplets from aerosol by evaporating the water and leaving behind the particles to be measured and counted (Twohy and Anderson, 2008).

Also, the amount of time in cloud was much less than desired. For 2016, there were a total of 101.1 hours of flight time, with in-cloud level legs occupying 15,040 seconds, or ~251 minutes, which is ~4.2 hours. While we were able to gather a few hours of cloud data, more is needed to properly analyze the horizontal structure of clouds. Over the course of the 15,040 seconds, nearly 1,956 km of horizontal cloud measurements were taken. It seems like big measurement, but not when compared to the over 6 million square kilometers of area that the MSc encompasses.

5.3 Future Work

As mentioned previously, this is a preliminary investigation into the microphysical properties of MSc in the SEA region. This is an ongoing field project that spans three consecutive years: 2016, 2017, 2018 for the months of September, August, and October, respectively. At this time, only the data from 2016 is available for analysis. Data from all three years will need to be analyzed in order to have a better understanding of the ACI within these

unique MSc. In addition, a comparison between the months will be useful for understanding the biomass burning season and the fluctuations of aerosol present in the atmosphere.

Another useful analysis would be to compare the cloud microphysical property results from the FPDR-PDI to the suite of cloud probe instruments from the University of North Dakota. It is advantageous to have data from two separate cloud instrument suites for validation of the observational *in-situ* cloud measurements.

Lastly, having the CVI inlet will allow for quantitative measurements of in-cloud aerosol and CCN, which was provided in the 2017 deployment. CCN measurements will be able to be used at value instead of as a proxy for "clean" or "polluted" clouds like what has been done in this work for 2016.

Date /Leg	Average Altitude (ft)	Average Altitude (m)	BC ($\mu g/m^3$)	Median Diameter (µm)	Effective Radius (µm)	LWC (g/m^3)	TNC (#/cc)
			0	**-**	**450**	**m**	
9_20_L1	753	230	12.62	10.33	10.58	0.500	410
9_06_L4	1096	334	2.982	20.1	12.38	0.932	140
9_20_L2	1105	337	6.291	16	10.35	0.926	331
9_24_L2	1473	449	95.81	5.6	3.62	0.012	77
Mean	1107	337	29.43	13.01	9.23	0.593	240
			450	**-**	**600**	**m**	
9_20_L3	1584	482	34.56	15.99	10.36	1.163	393
9_14_L2	1839	561	1.498	11.03	8.84	0.378	347
9_14_L1	1964	599	1.328	14.02	9.7	0.481	255
Mean	1796	547	12.46	13.68	9.63	0.674	331
			600	**-**	**750**	**m**	
9_04_L1	2010	613	7.514	17.14	14.09	0.769	135
9_06_L2	2038	621	42.09	12.82	8.3	0.407	285
9_14_L4	2262	689	1.159	15.81	10.31	0.714	255
9_10_L1b	2318	707	1.488	9.38	12.89	0.096	83
9_10 L1a	2320	707	1.999	9.74	6.91	0.116	28
9_02_L1	2321	707	21.81	12.11	10.67	0.404	237
9_14_L3	2339	713	1.302	16.11	10.8	0.736	238
9_12_L2	2340	713	10.59	8.29	10.64	0.074	67
9_25_L2	2452	747	1.412	17.88	17.38	0.830	123
Mean	2267	691	9.929	13.25	11.33	0.461	161
			750	**-**	**900**	**m**	
8_31_L3	2549	777	45.93	12.8	8.27	0.722	514
8_31_ L1	2555	779	65.61	11.73	9.38	0.578	415

9_06_L1	2583	787	4.672	11.57	8.36	0.446	385
9_06_L3	2596	791	53.6	16.83	10.76	0.848	244
9_25_L1	2603	793	4.65	13.34	15.24	0.463	163
9_27_L1b	2613	796	1.721	24.78	16.68	0.902	48
9_27_L1a	2621	799	7.752	24.61	21.57	2.153	118
9_04_L2	2867	874	14.65	19.39	13.69	0.937	170
8_31_L2	2870	875	44.42	14.46	10.8	0.821	334
Mean	2647	807	27	17.42	13.32	0.922	246
			900	**-**	**1100**	**m**	
9_10_L4	3013	918	1.338	14.97	12.49	0.557	169
9_10_L3	3101	945	10.18	14.73	10.76	0.496	205
9_10_L2	3135	956	1.028	15.89	12.05	0.697	192
9_24_L3	3212	979	136.68	8.11	8.66	0.058	121
9_18_L1	3217	981	21.62	16.29	12.02	0.703	180
9_12_L1	3255	992	2.191	17.13	16.92	0.702	159
9_24_L4	3519	1073	126.67	14.51	11.33	0.532	217
9_24_L1	3572	1089	87.39	10.71	7.08	0.277	309
Mean	3253	992	48.39	14.04	11.41	0.503	194

Table 1. For every level leg, shown in the left bolded column, averaged cloud properties are listed and sorted by altitude groups with the mean of each found at the bottom.

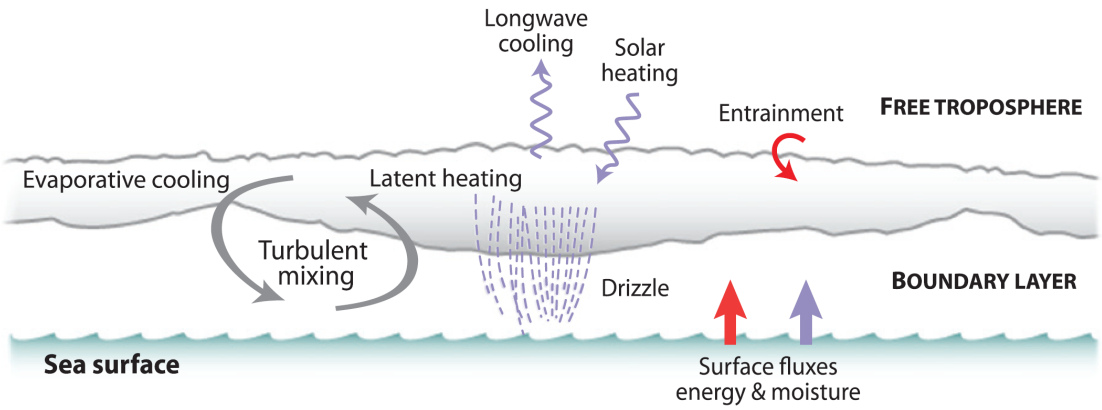

Figure 1. Schematic of the key processes influencing MSc formation. Borrowed from Wood et al., 2012.

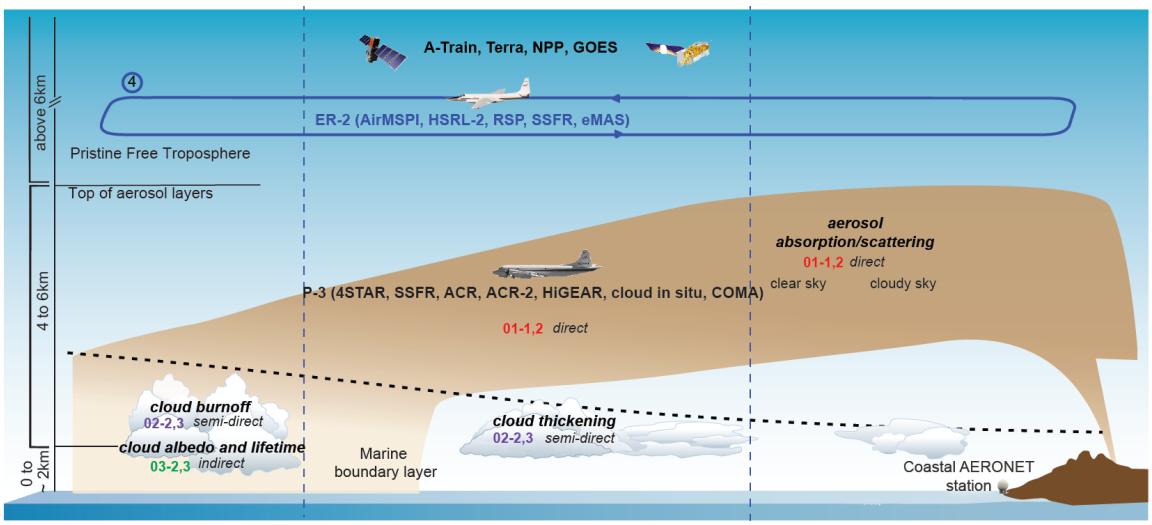

Figure 2. Schematic showing the original idea of how the smoke (light brown) is advected over the SEA, and how it may possibly interact with the coastal clouds (Redemann et al., 2014)

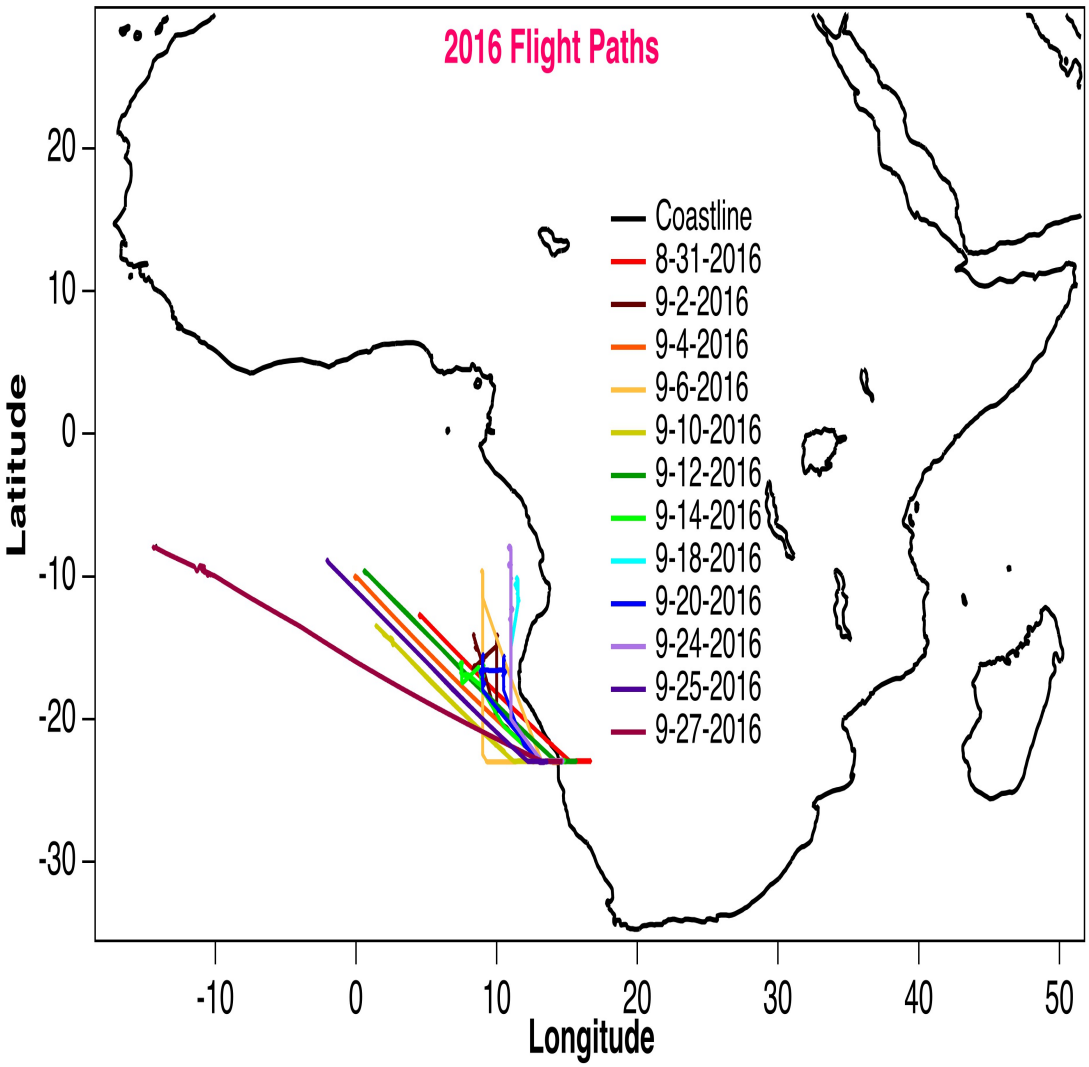

Figure 3. Flight paths during the 2016 ORACLES deployment to Namibia. Each flight is color-coded. Diagonal offset lines are the RF. Variable lines are the TOOF.

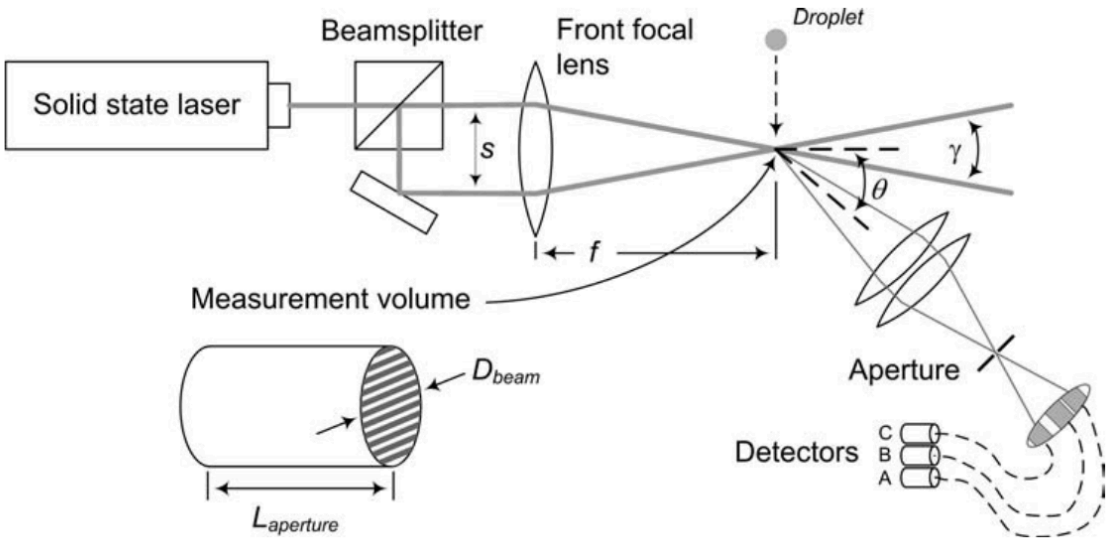

Figure 4. Schematic of the basic PDI principals. A solid laser is split into two equal intensity beams by the beamsplitter, and is then brought to an intersection point by the front focal lens where the droplet will be detected. The scattered light is then transmitted by the aperture onto three detectors: A, B, and C (Chuang et al., 2008).

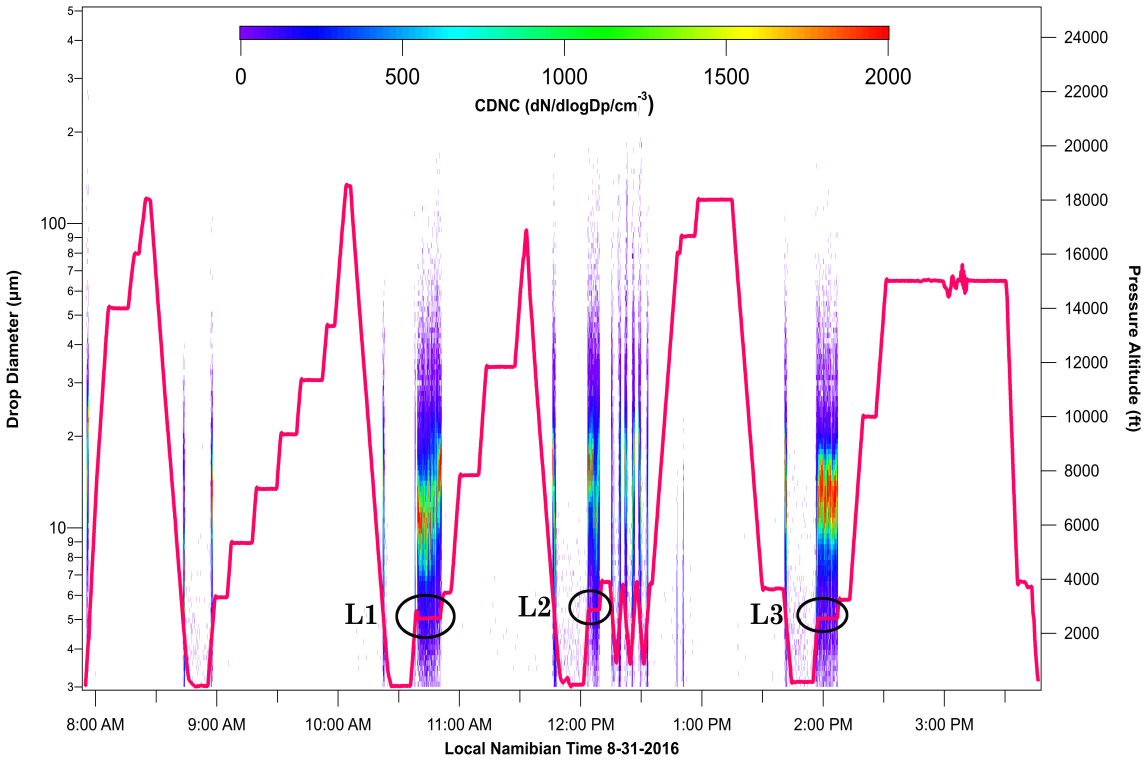

Figure 5. "Rainbow Plot" displaying drop diameter (µm) on the left axis, local Namibian time on the bottom axis, and pressure altitude (ft) on the right axis. The rainbow colors are the cloud drop number concentrations as represented in the color bar, the pink line shows where the plane flew in pressure altitude, and the black circles indicate level cloud legs during the flight. For this particular flight, there were three level cloud legs labeled L1, L2, and L3.

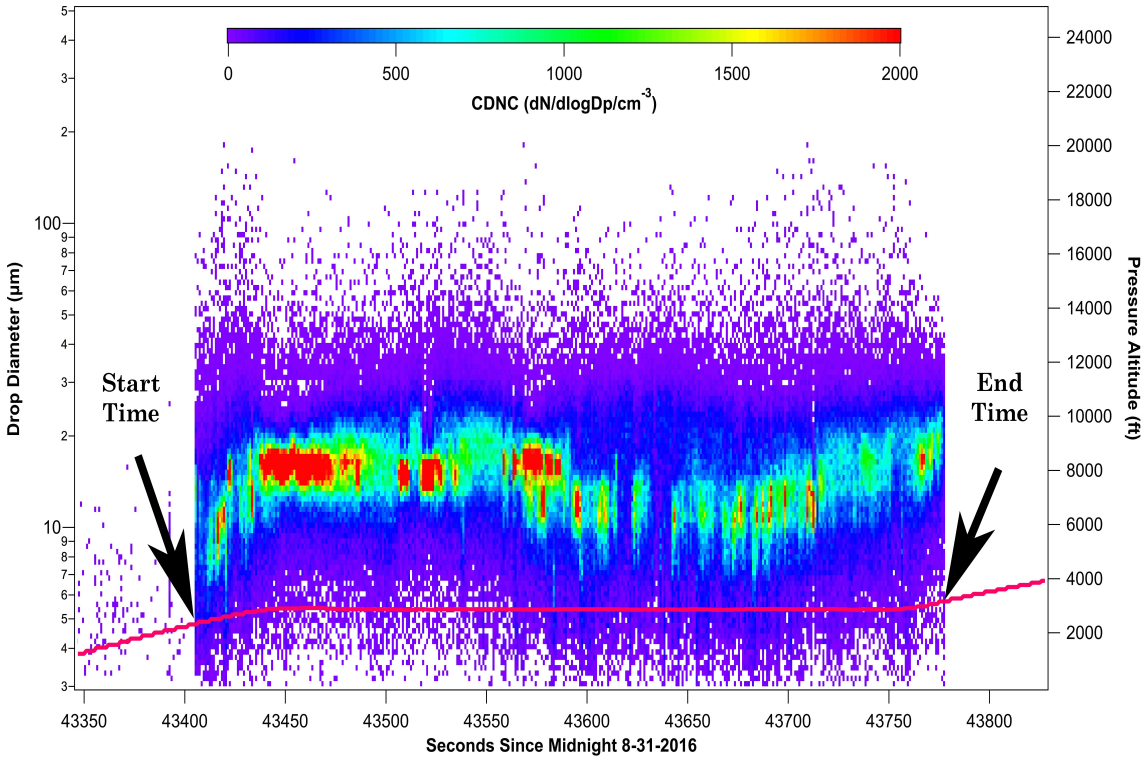

Figure 6 is the same as Figure 5, but has been zoomed in on L2 with seconds since midnight to easily to show how we found the start and end times for each level leg as indicated in the figure by black arrows.

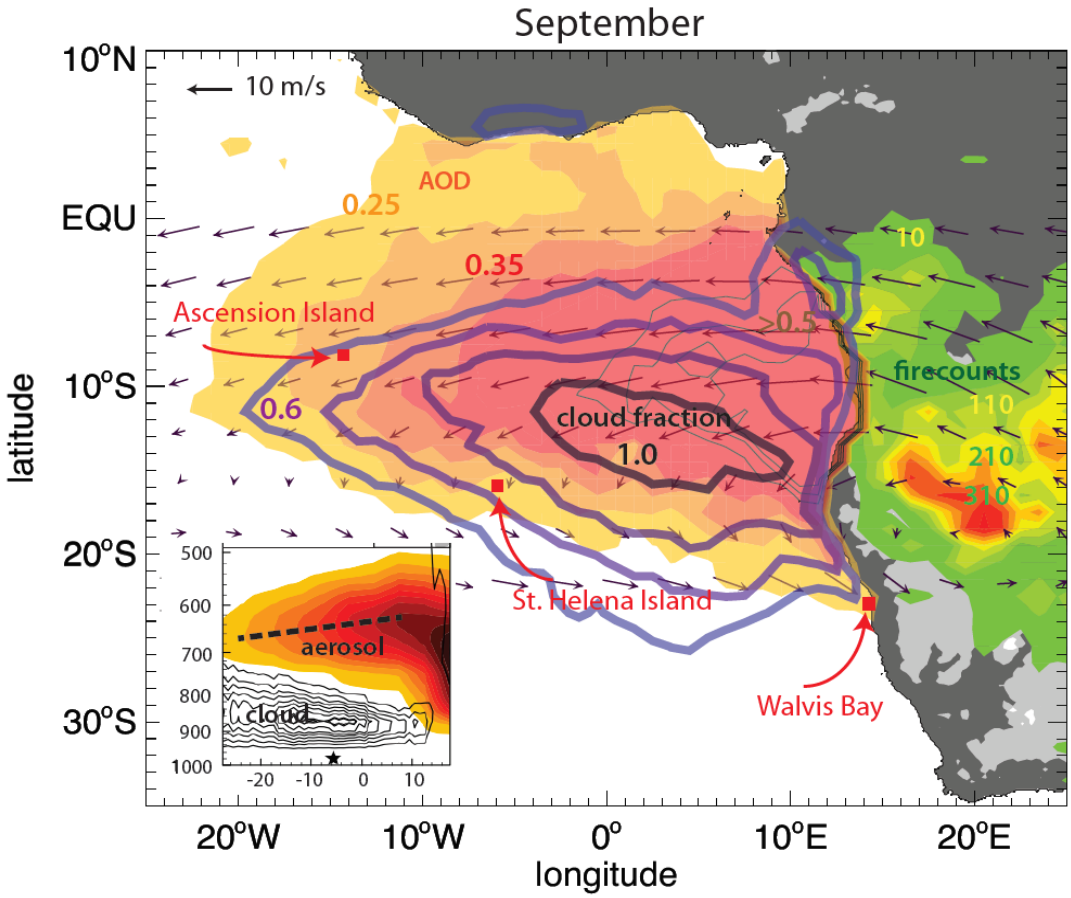

Figure 7 is Figure 3.1-1 taken from Redemann et al. 2014. The main figure is showing the BBA plume as the warm, red colors being transported westward over the SEA. The green with red is showing the fire counts. The blue contours represent cloud fractions. The data for the main figure was gathered from MODIS. The inlet figure shows the BBA as warm to dark red and the MSc as grey and the data was gathered from CALIOP and CloudSat.

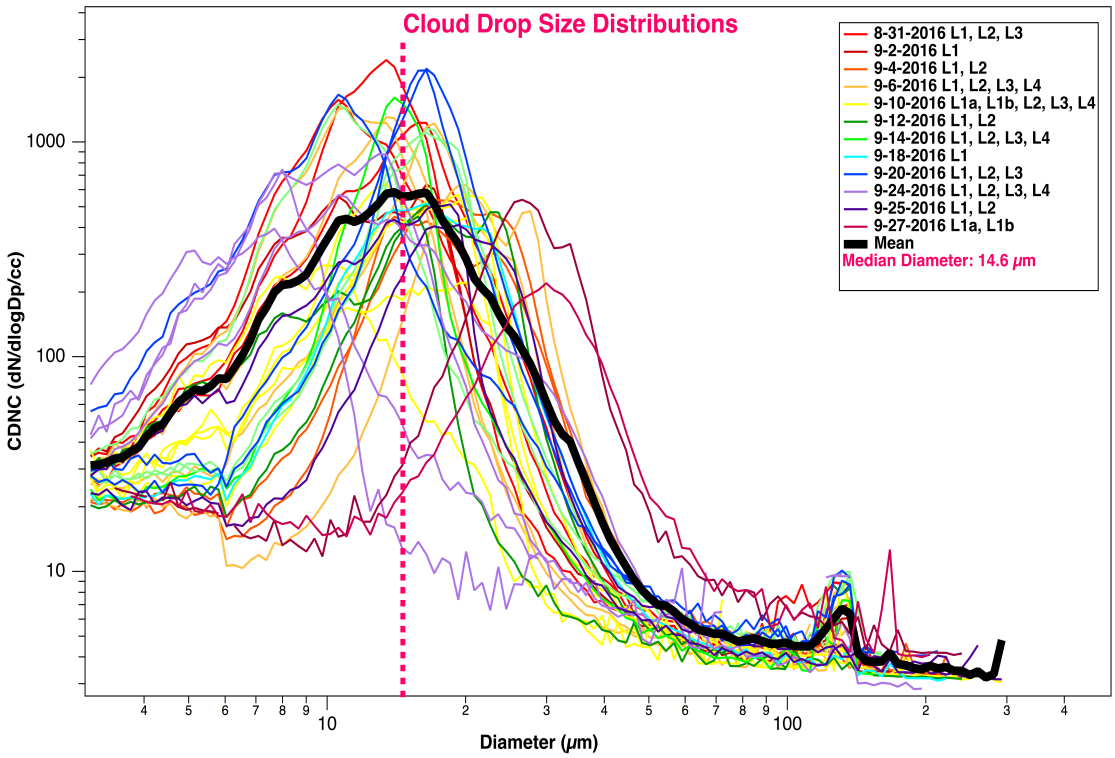

Figure 8 shows the cloud drop size distributions for all of the level legs in 2016 with the CDNC on the left axis and the droplet diameter (μm) on the bottom axis as a log-log scale. Each flight is color coded, with the mean of all of the level legs combined displayed as a thick black line. The pink dotted line represents the median diameter.

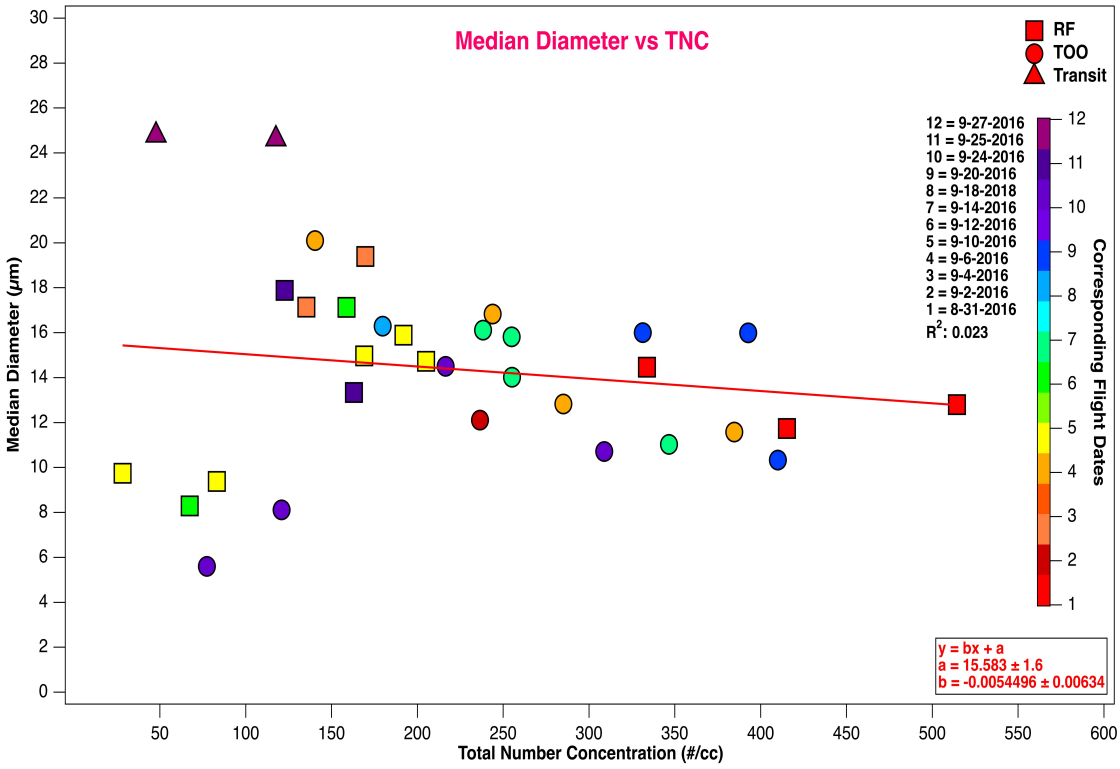

Figure 9. Median diameter (μm) as a function of total number concentration (#/cc) for all level legs in 2016. Each flight is color-coded to a corresponding number on the color bar. The red line is the trend line. Squares represent TF, circles represent TOO, and triangles represent the Transit legs.

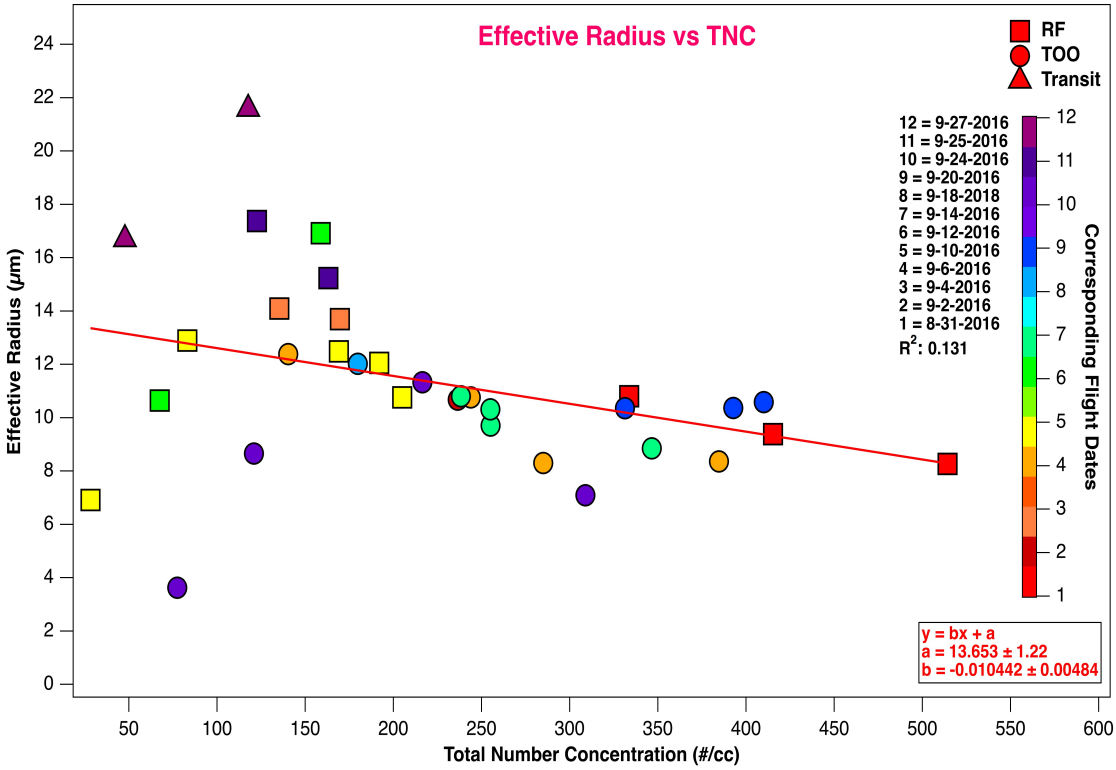

Figure 10. Effective radius (μm) as a function of the total number concentration (#/cc) for all level legs in 2016. Each flight is color-coded to a corresponding number on the color bar. The red line is the trend line. Squares represent TF, circles represent TOO, and triangles represent the Transit legs.

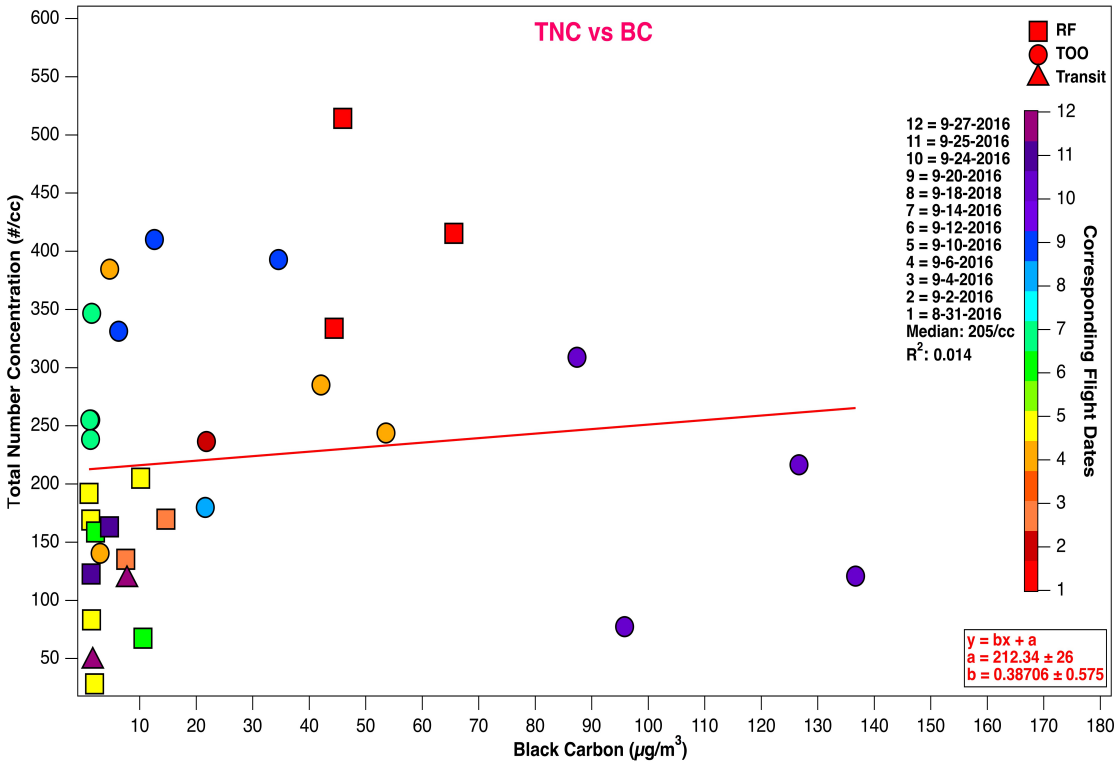

Figure 11. TNC (#/cc) as a function of BC (μg/m^3) for all level legs in 2016. Each flight is color-coded to a corresponding number on the color bar. The red line is the trend line. Squares represent TF, circles represent TOO, and triangles represent the Transit legs.

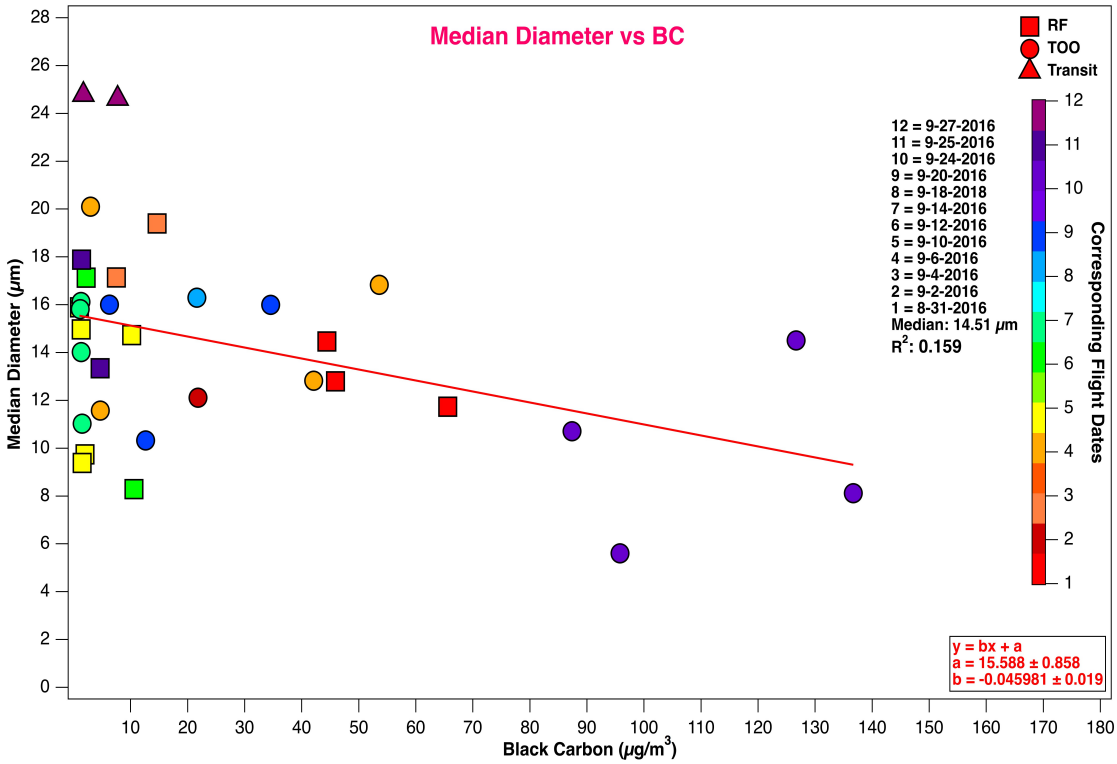

Figure 12. Median diameter (µm) as a function of BC (µg/m^3) for all level legs in 2016. Each flight is color-coded to a corresponding number on the color bar. The red line is the trend line. Squares represent TF, circles represent TOO, and triangles represent the Transit legs.

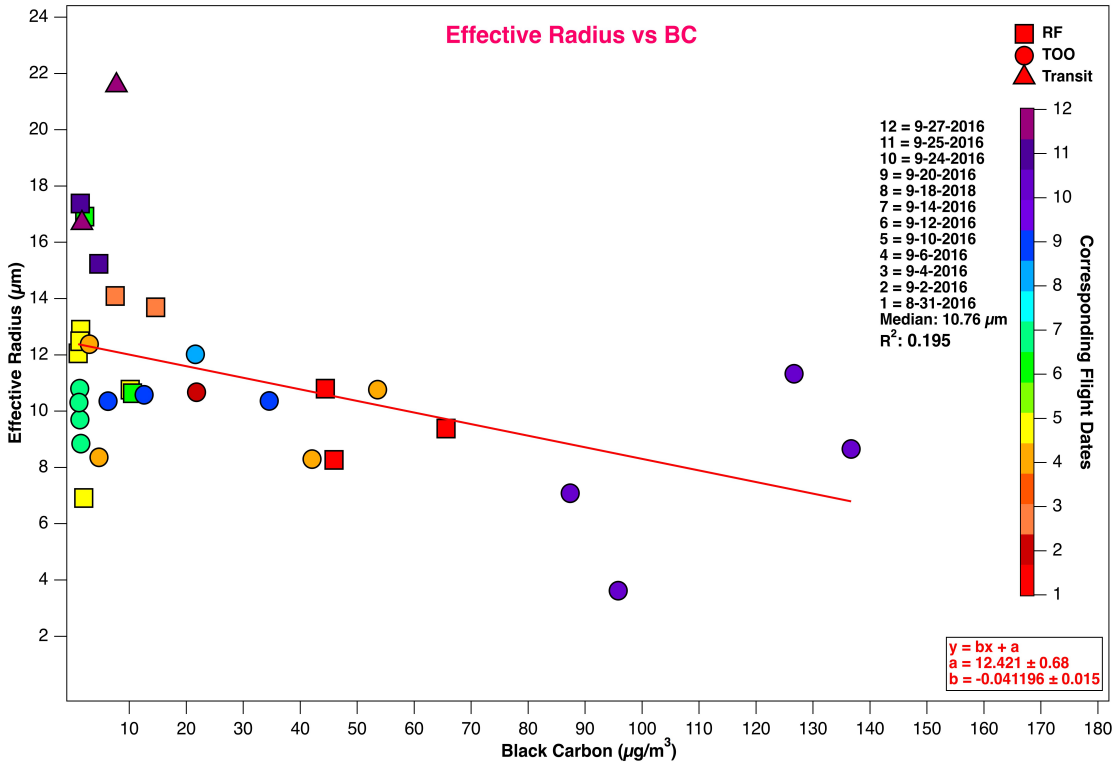

Figure 13. Effective radius (µm) as a function of BC (µg/m^3) for all level legs in 2016. Each flight is color-coded to a corresponding number on the color bar. The red line is the trend line. Squares represent TF, circles represent TOO, and triangles represent the Transit legs.

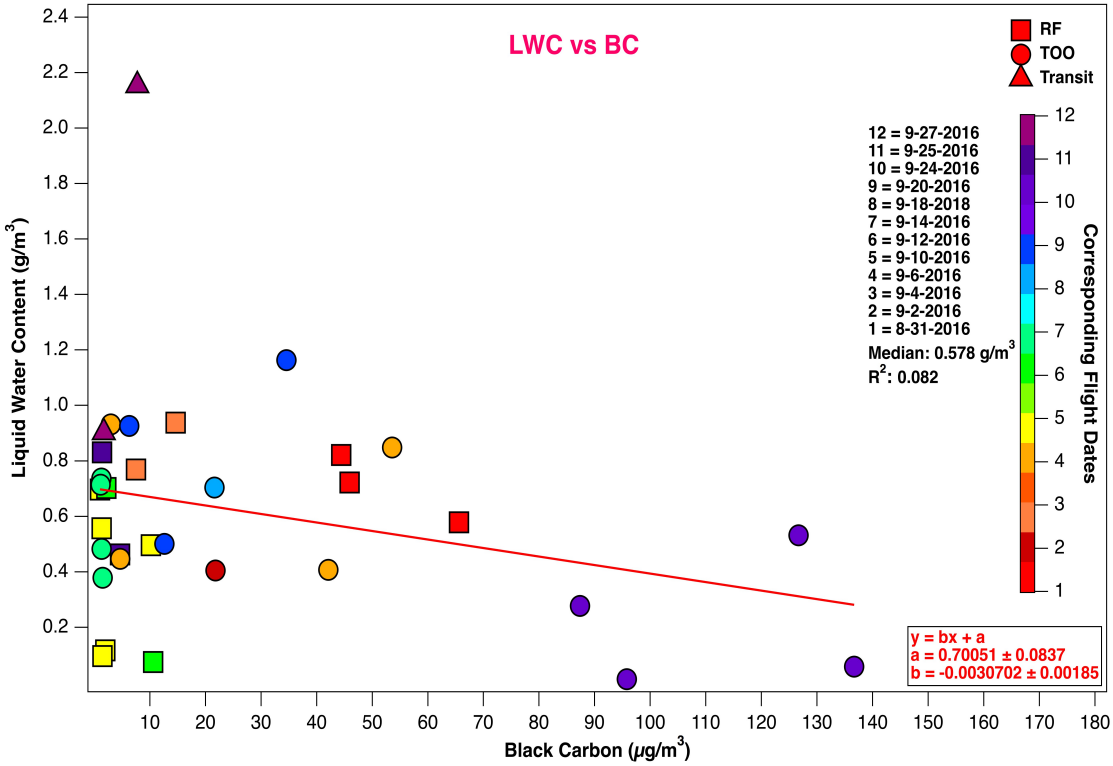

Figure 14. Liquid water content (g/m^3) as a function of BC (µg/m^3) for all level legs in 2016. Each flight is color-coded to a corresponding number on the color bar. The red line is the trend line. Squares represent TF, circles represent TOO, and triangles represent the Transit legs.

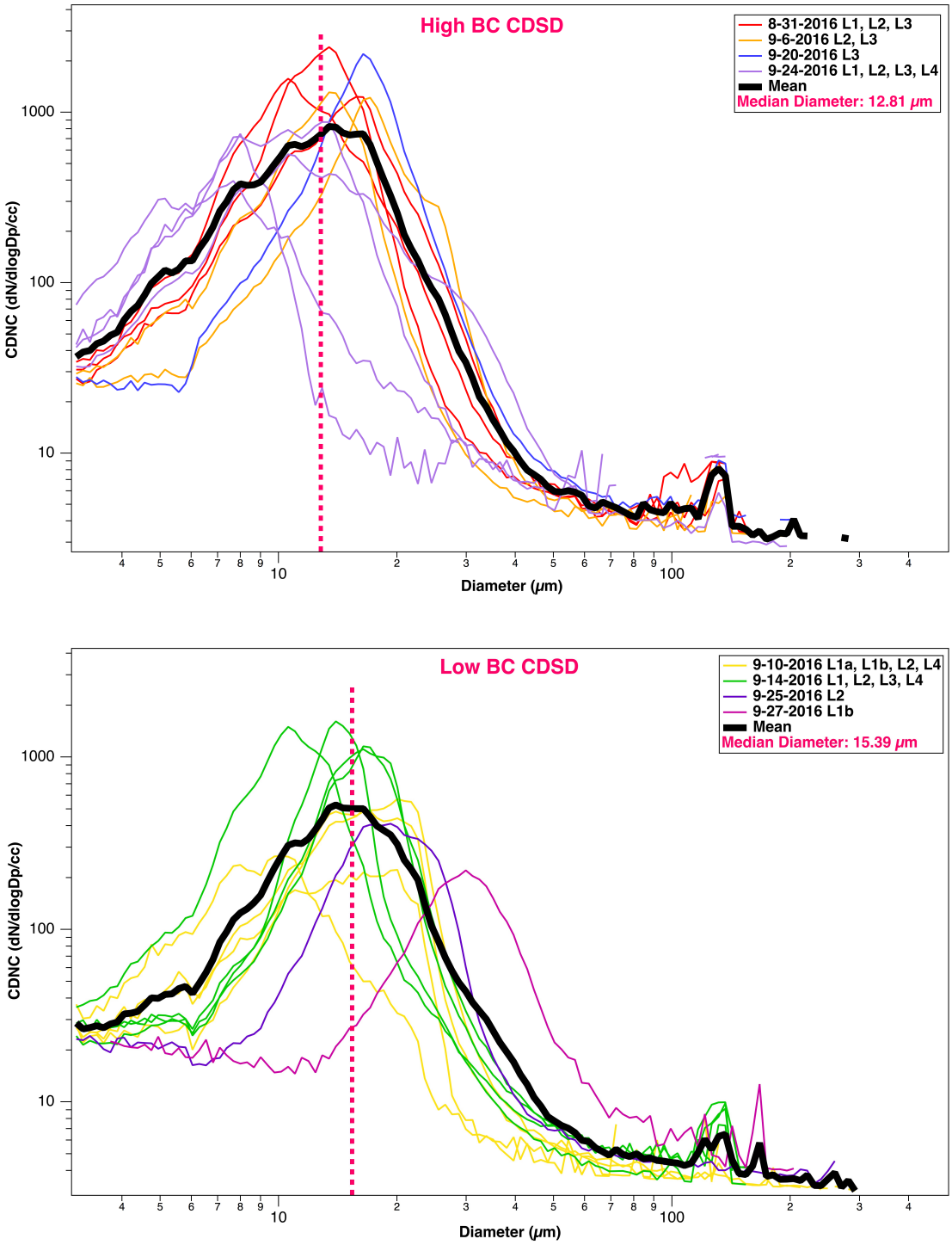

Figure 15 shows the cloud drop size distributions for the high BC legs (top) and low BC legs (bottom). CDNC is on the left axis and the droplet diameter (μm) is on the bottom axis as a log-log scale. Each flight is color coded with the mean of the high BC level legs displayed as a thick black line. The pink dotted line represents the median diameter.

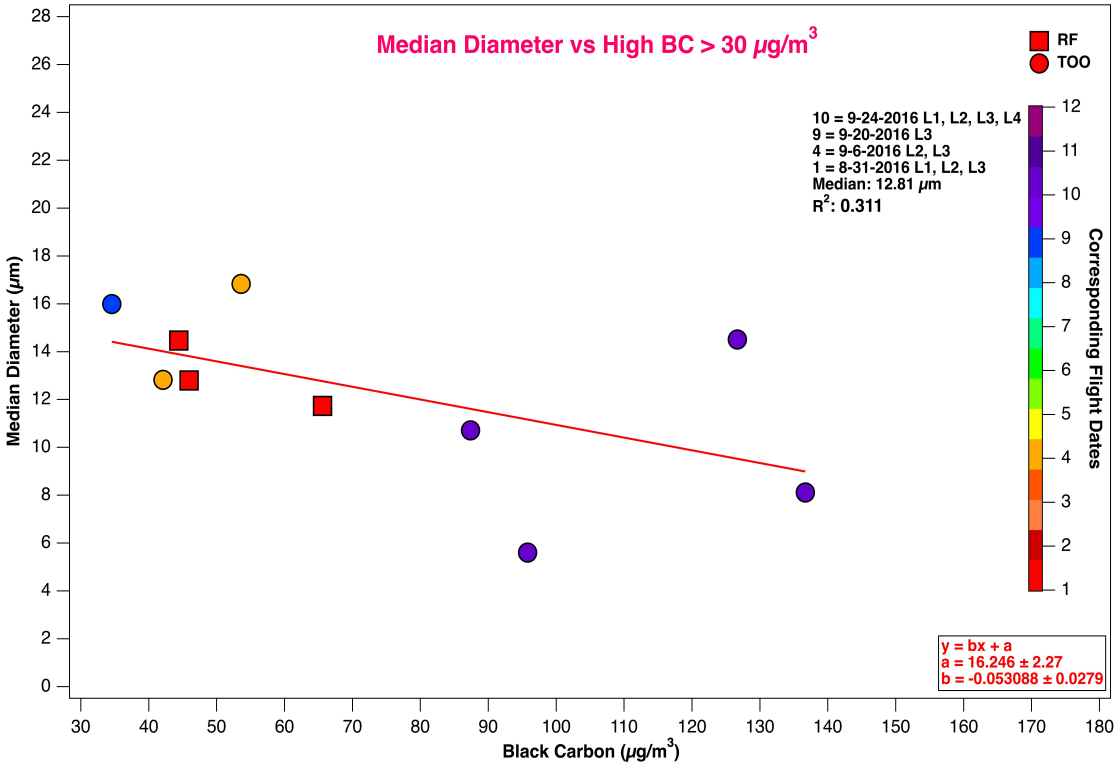

Figure 16. Median diameter (µm) as a function of BC (µg/m^3) for the level legs with CCN values greater than 30 µg/m^3. Each flight is color-coded to a corresponding number on the color bar. Squares represent TF and circles represent TOO.

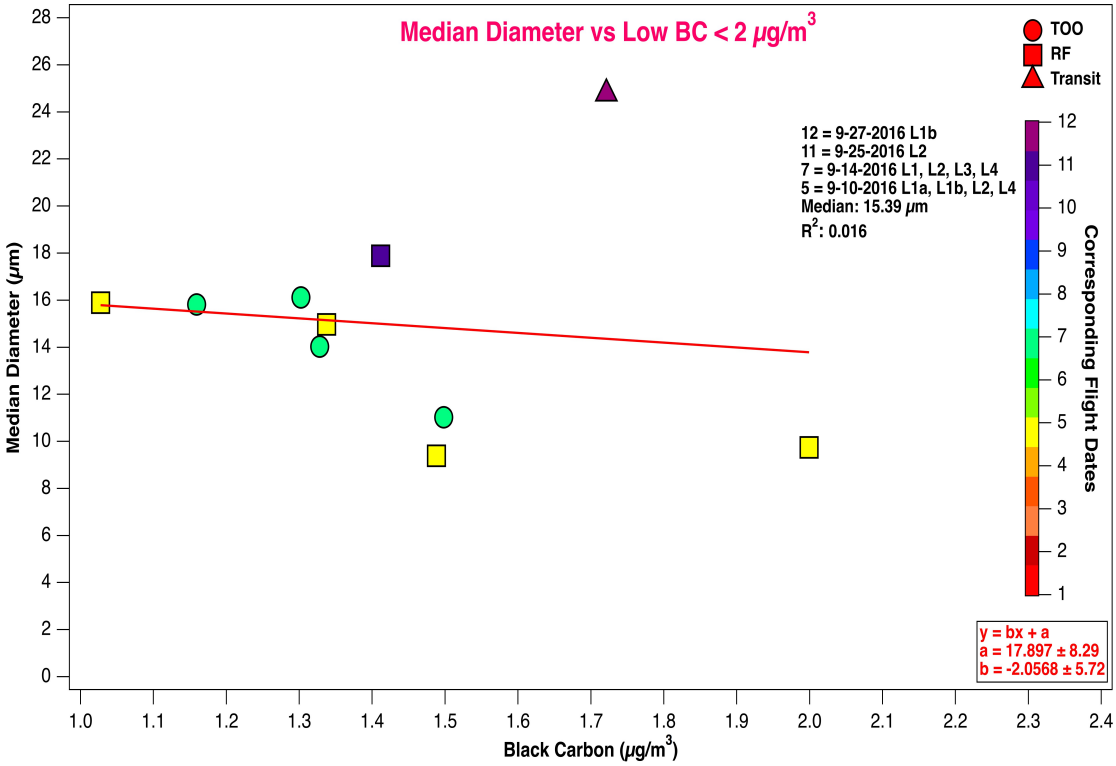

Figure 17. Median diameter (µm) as a function of BC (µg/m^3) for the level legs with BC values less than 2 µg/m^3. Each flight is color-coded to a corresponding number on the color bar. The red line is the trend line. Squares represent TF, circles represent TOO, and triangles represent the Transit legs.

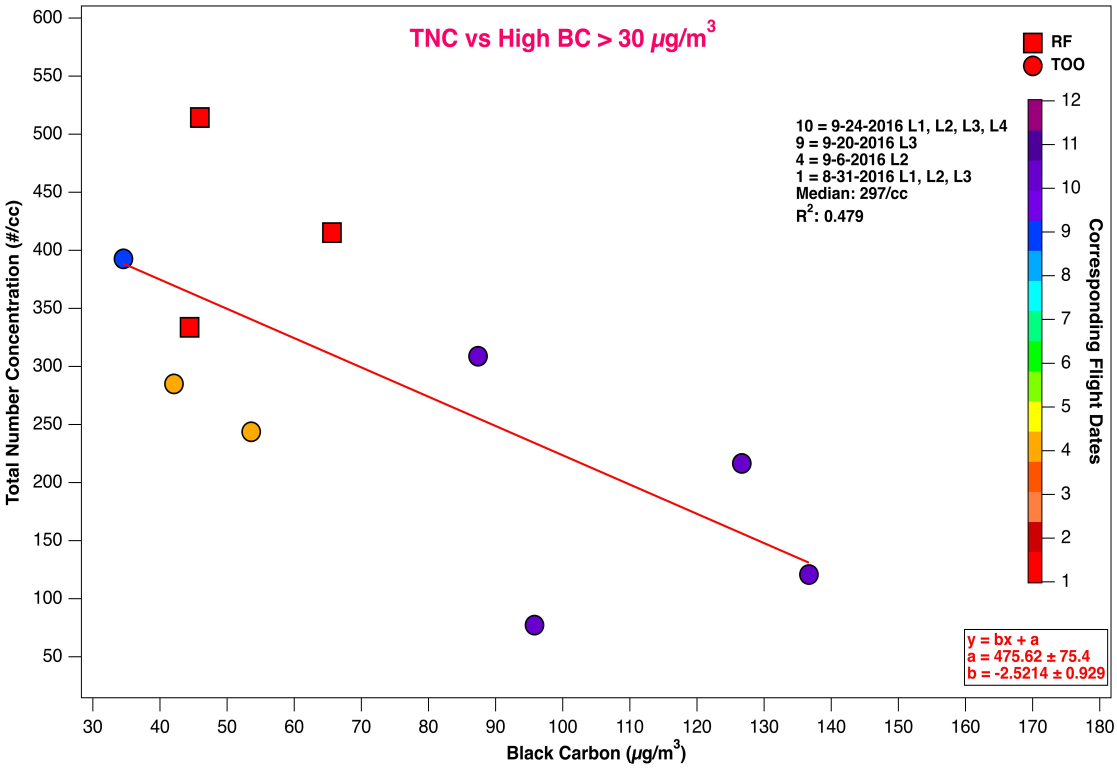

Figure 18. TNC (#/cc) as a function of BC (µg/m^3) for the level legs with BC values greater than 30 µg/m^3. Each flight is color-coded to a corresponding number on the color bar. The red line is the trend line. Squares represent TF and circles represent TOO.

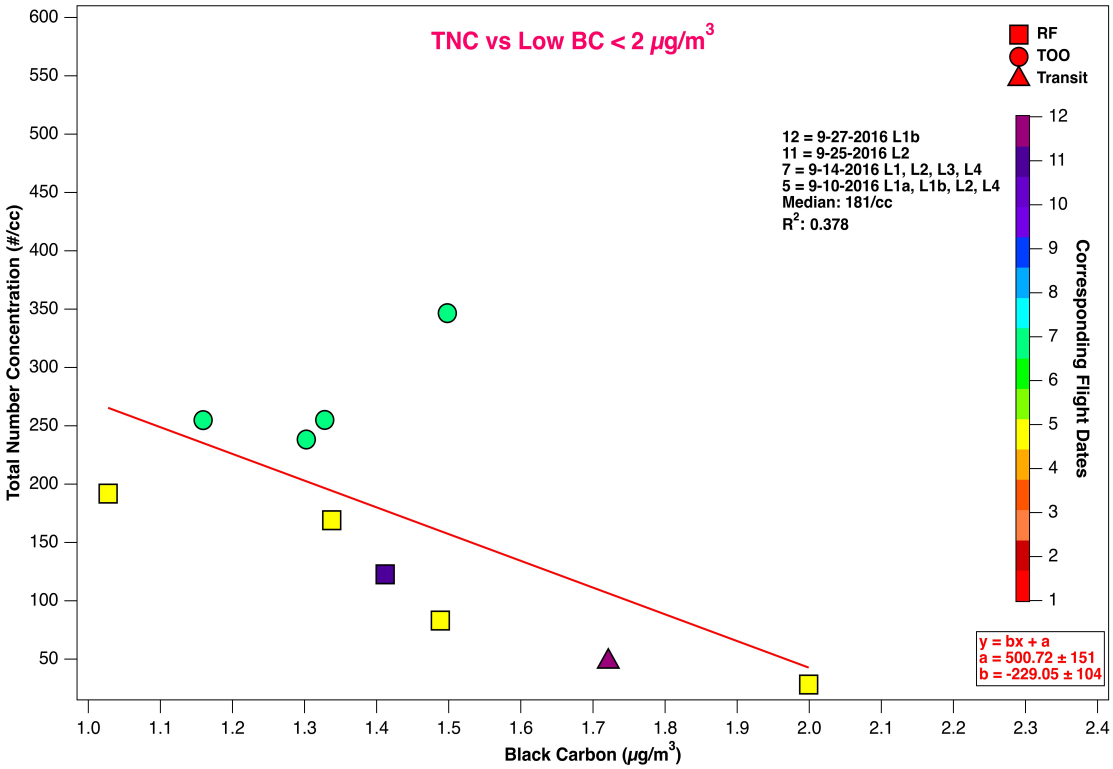

Figure 19. TNC (#/cc) as a function of BC (µg/m^3) for the level legs with BC values less than 2 µg/m^3. Each flight is color-coded to a corresponding number on the color bar. The red line is the trend line. Squares represent TF, circles represent TOO, and triangles represent the Transit legs.

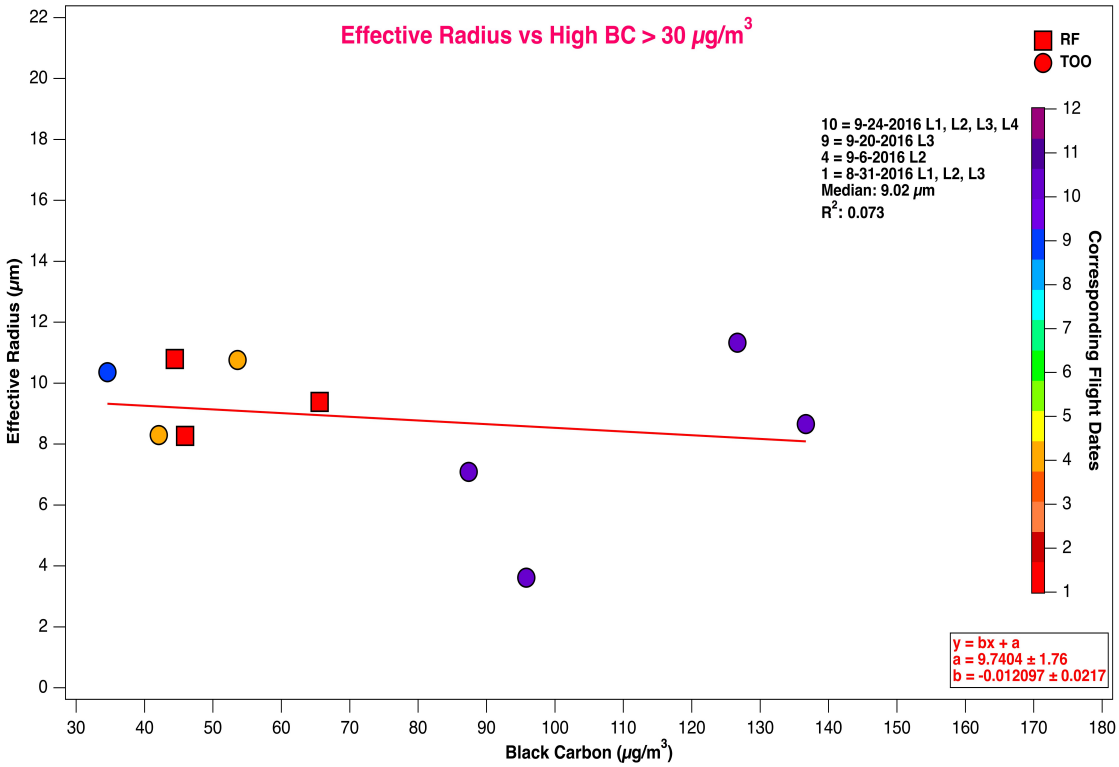

Figure 20. Effective radius (µm) as a function of BC (#/cc) for the level legs with BC values greater than 30 µg/m^3. Each flight is color-coded to a corresponding number on the color bar. The red line is the trend line. Squares represent TF and circles represent TOO.

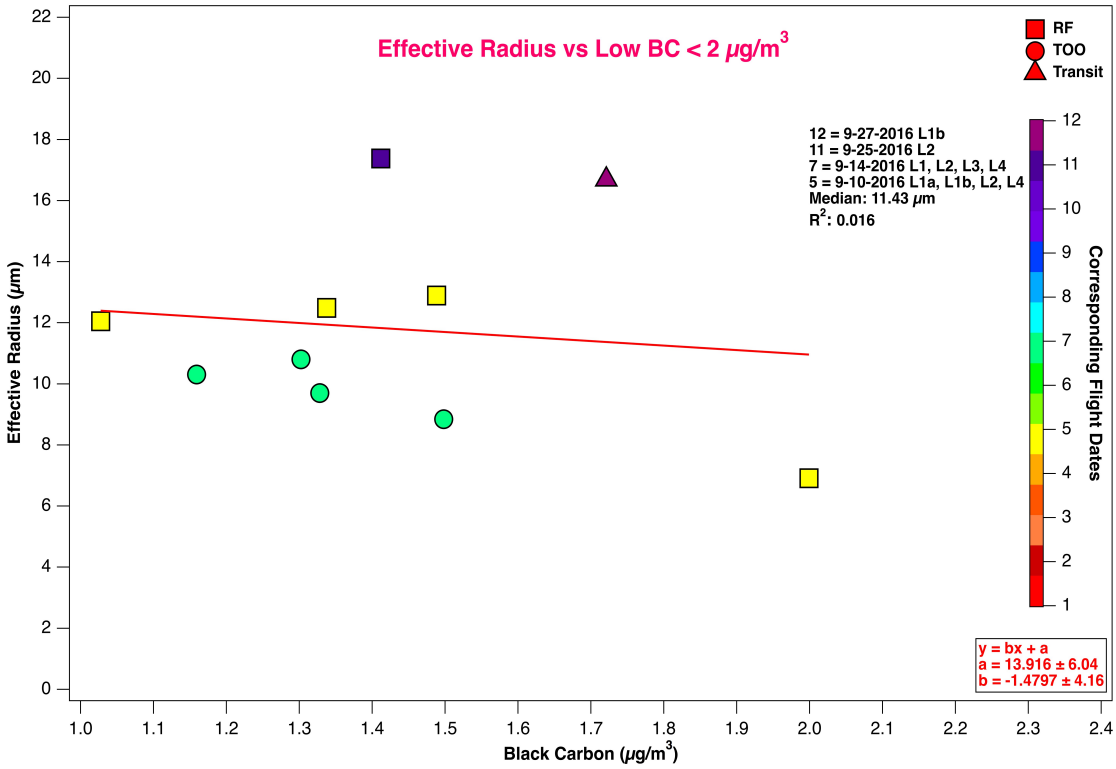

Figure 21. Effective radius (µm) as a function of BC (#/cc) for the level legs with BC values less than 2 µg/m^3. Each flight is color-coded to a corresponding number on the color bar. The red line is the trend line. Squares represent TF, circles represent TOO, and triangles represent the Transit legs.

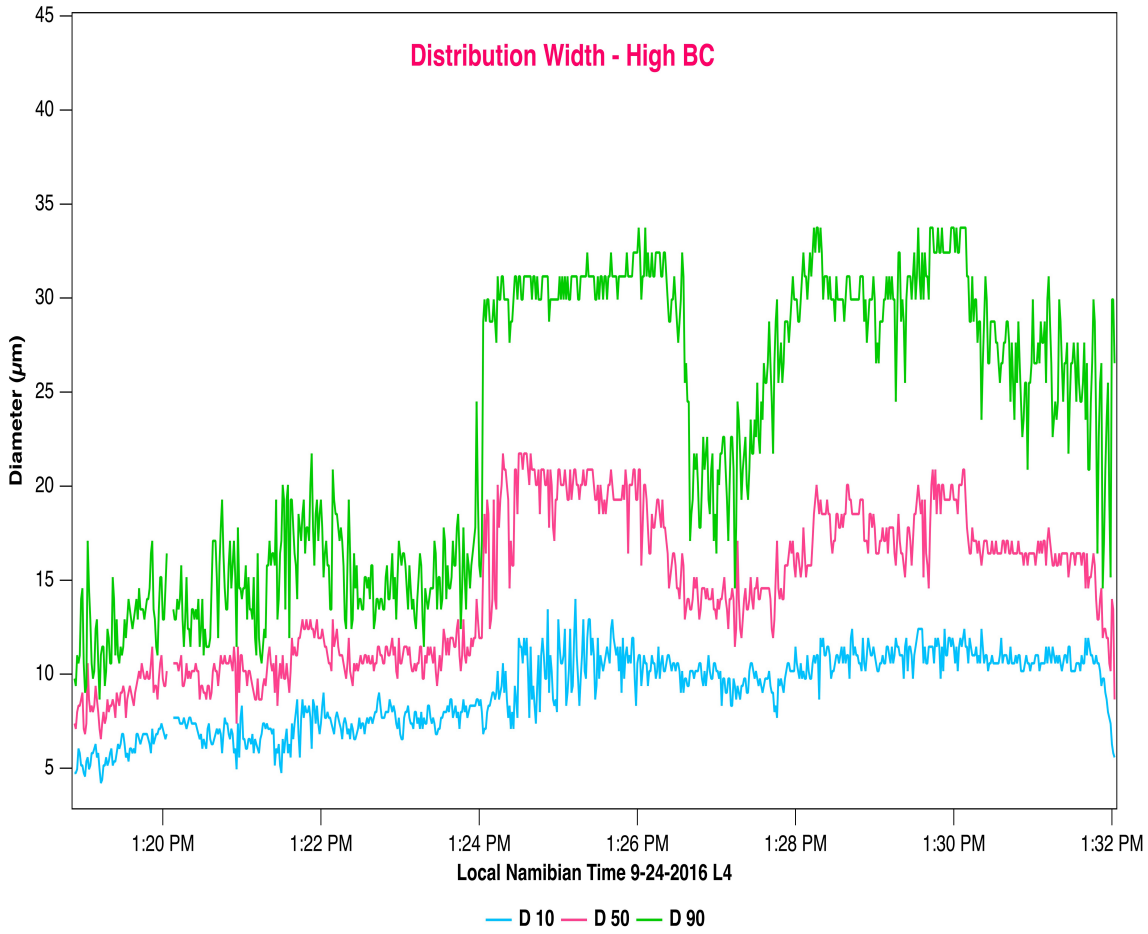

Figure 22. Droplet diameter (μm) as a function of local Namibian time for L4 on 9-24-2016. Displayed are the percentiles: cyan represents the 10th percentile, pink represents the 50th percentile, and green represents the 90th percentile. As a whole, this figure gives the distribution width for a level leg with a high BC value of 126.7 μg/m^3.

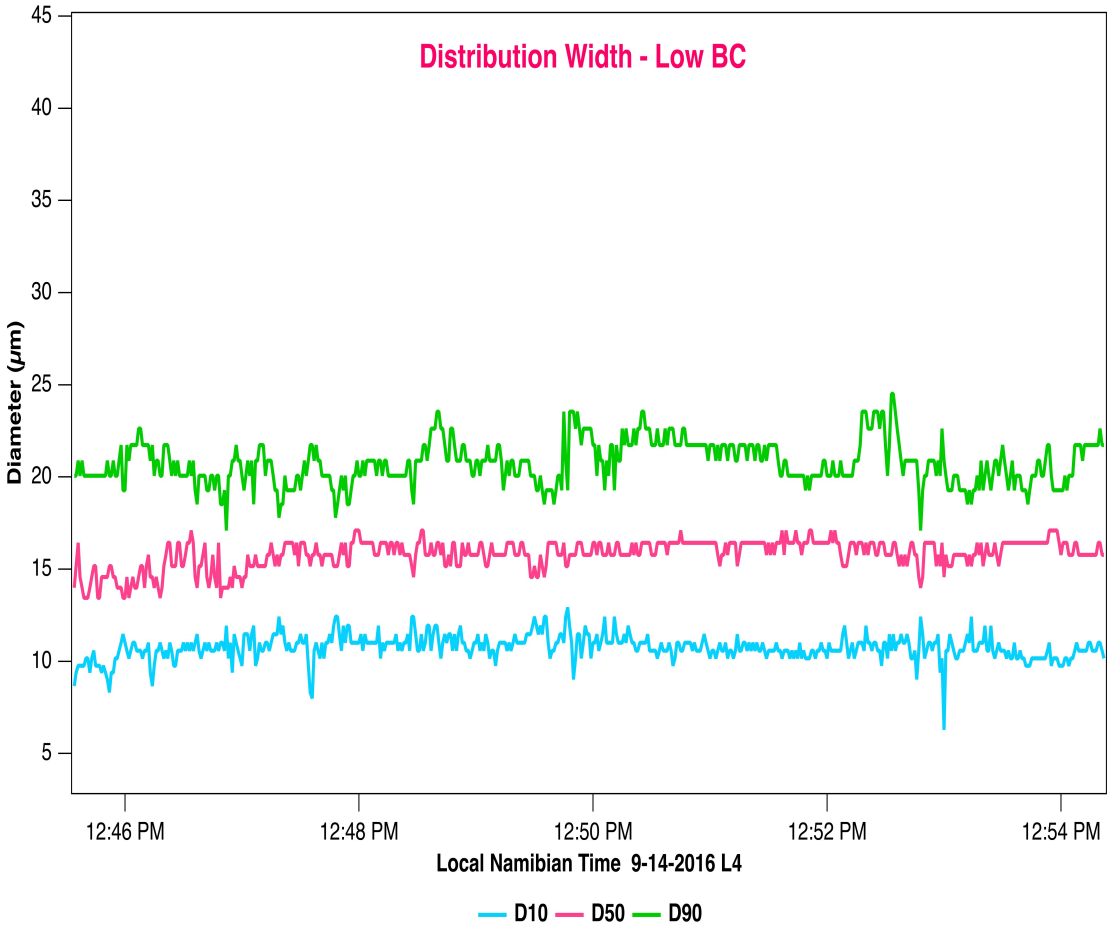

Figure 23. Droplet diameter (μm) as a function of seconds since midnight for L4 on 9-14-2016. Displayed are the percentiles: cyan represents the 10th percentile, pink represents the 50th percentile, and green represents the 90th percentile. As a whole, this figure gives the distribution width for a level leg with a low BC value of 1.16 μg/m^3.

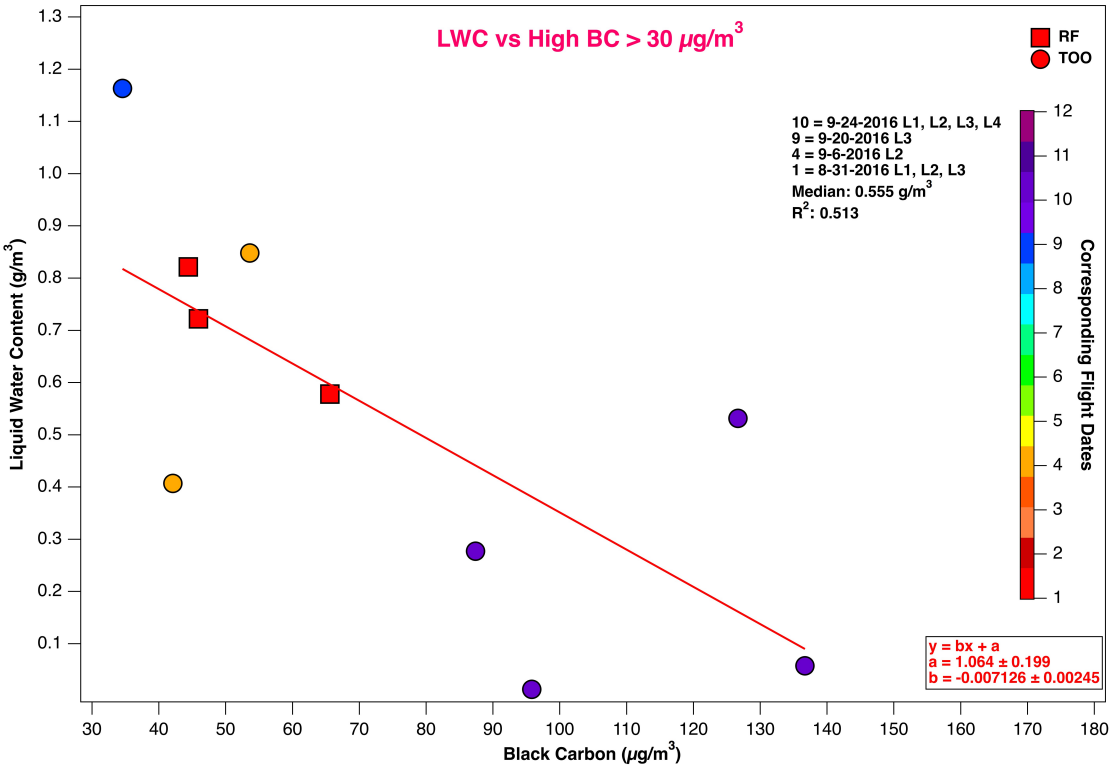

Figure 24. Liquid water content (g/m^3) as a function of BC (µg/m^3) for the level legs with BC values greater than 30 µg/m^3. Each flight is color-coded to a corresponding number on the color bar. The red line is the trend line. Squares represent TF and circles represent TOO.

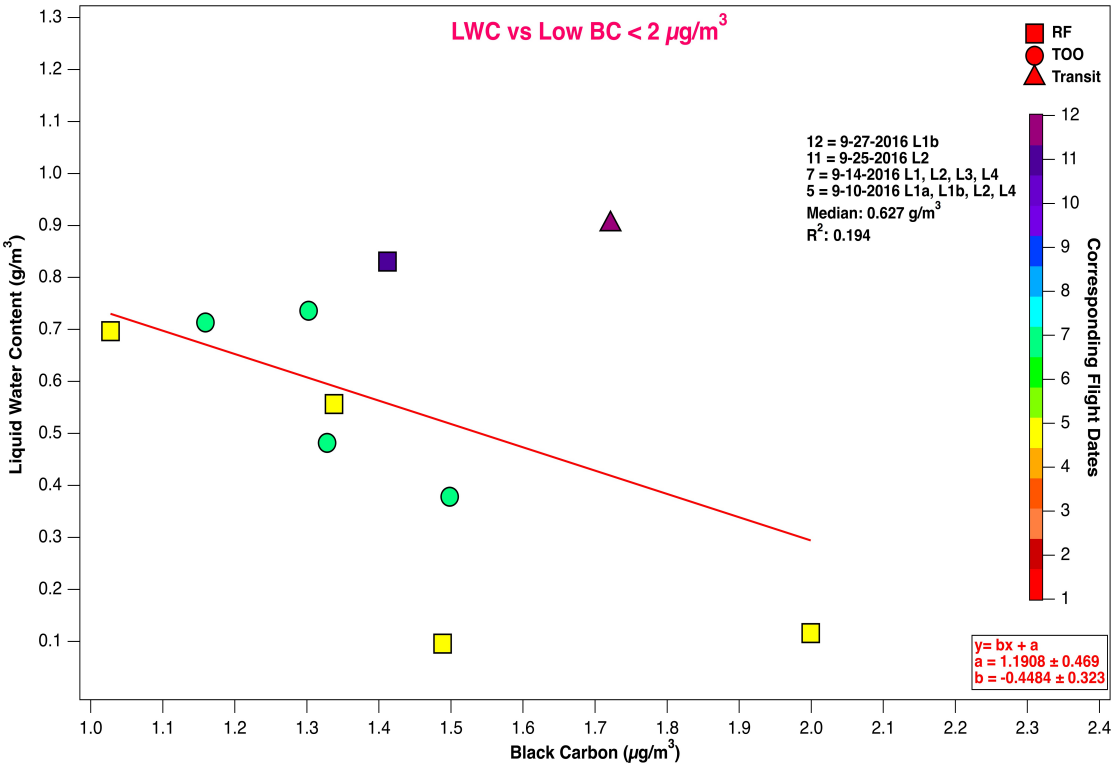

Figure 25. Liquid water content (g/m^3) as a function of BC (µg/m^3) for the level legs with BC values less than 2 µg/m^3. Each flight is color-coded to a corresponding number on the color bar. The red line is the trend line. Squares represent TF, circles represent TOO, and triangles represent the Transit legs.

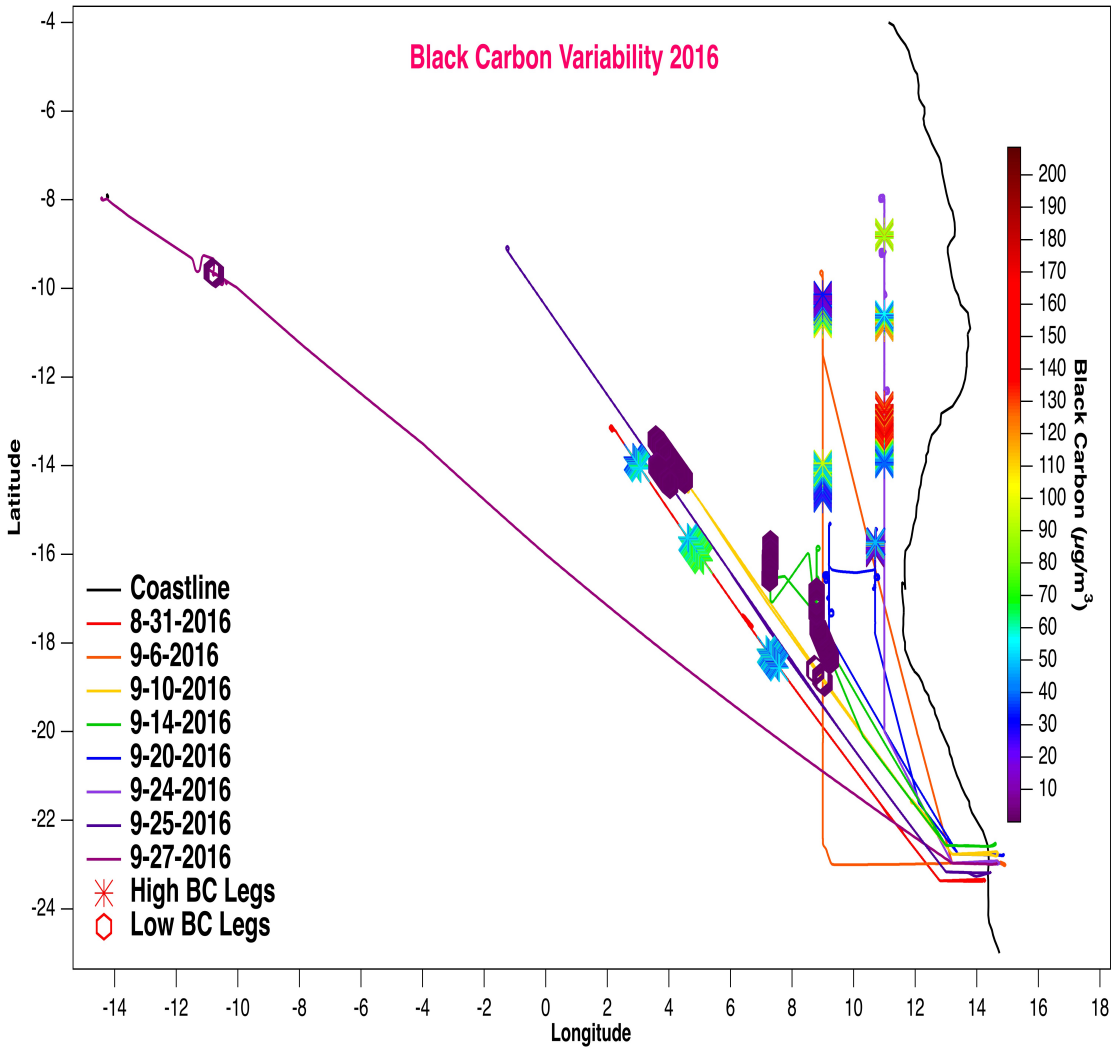

Figure 26 gives the variability of BC during the 2016 level legs with latitude on the left and longitude on the bottom. The west coast of Africa can be seen by the solid black contour. Only the high BC (>30 µg/m^3) and low BC (<2 µg/m^3) threshold legs are shown The flight paths are color-coded by flight date. High BC legs are shown as asterisks, and low BC legs are shown as hexagons.

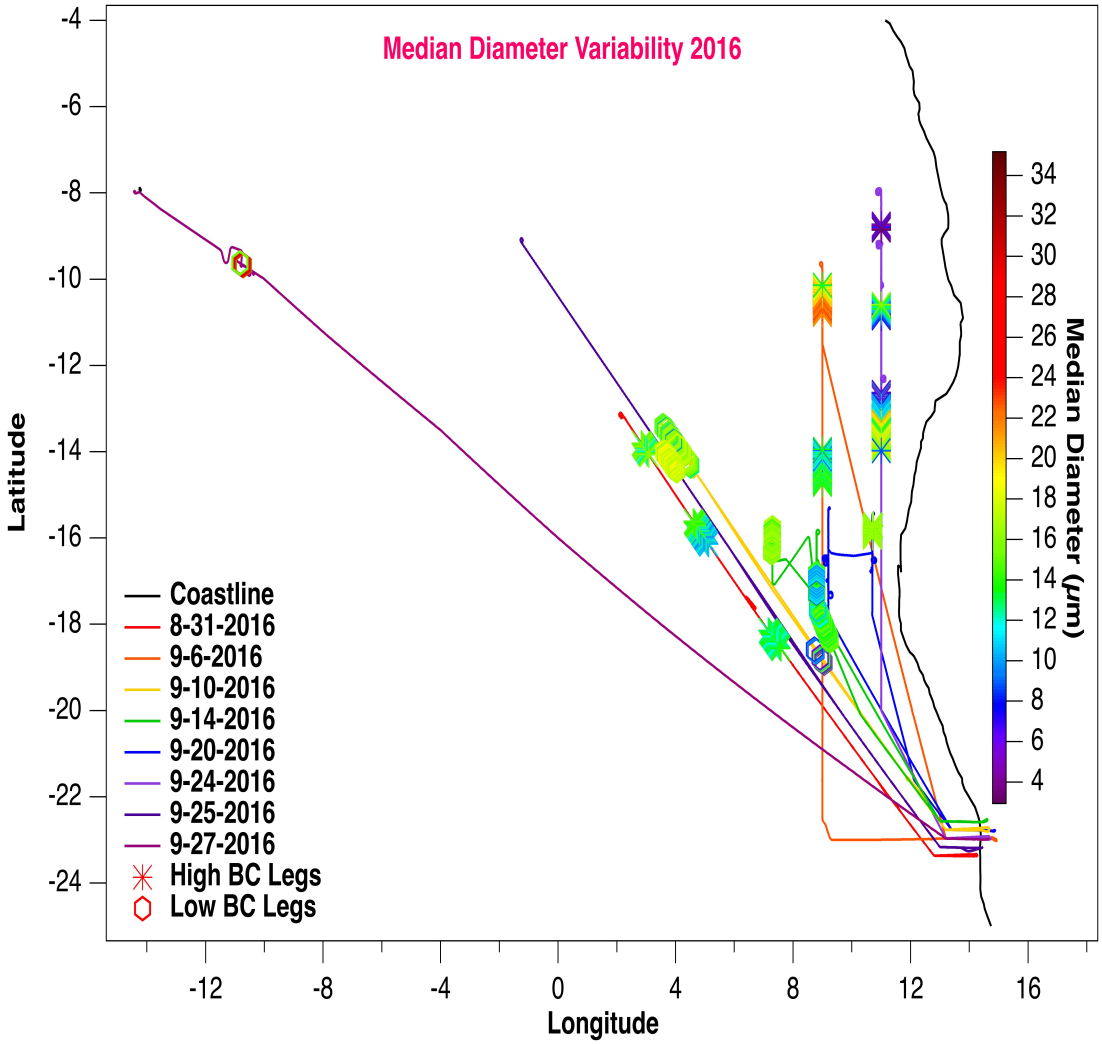

Figure 27 gives the variability of median diameter during the 2016 level legs with latitude on the left and longitude on the bottom. The west coast of Africa can be seen by the solid black contour. Only the high BC (>30 μg/m^3) and low BC (<2 μg/m^3) threshold legs are shown The flight paths are color-coded by flight date. High BC legs are shown as asterisks, and low BC legs are shown as hexagons.

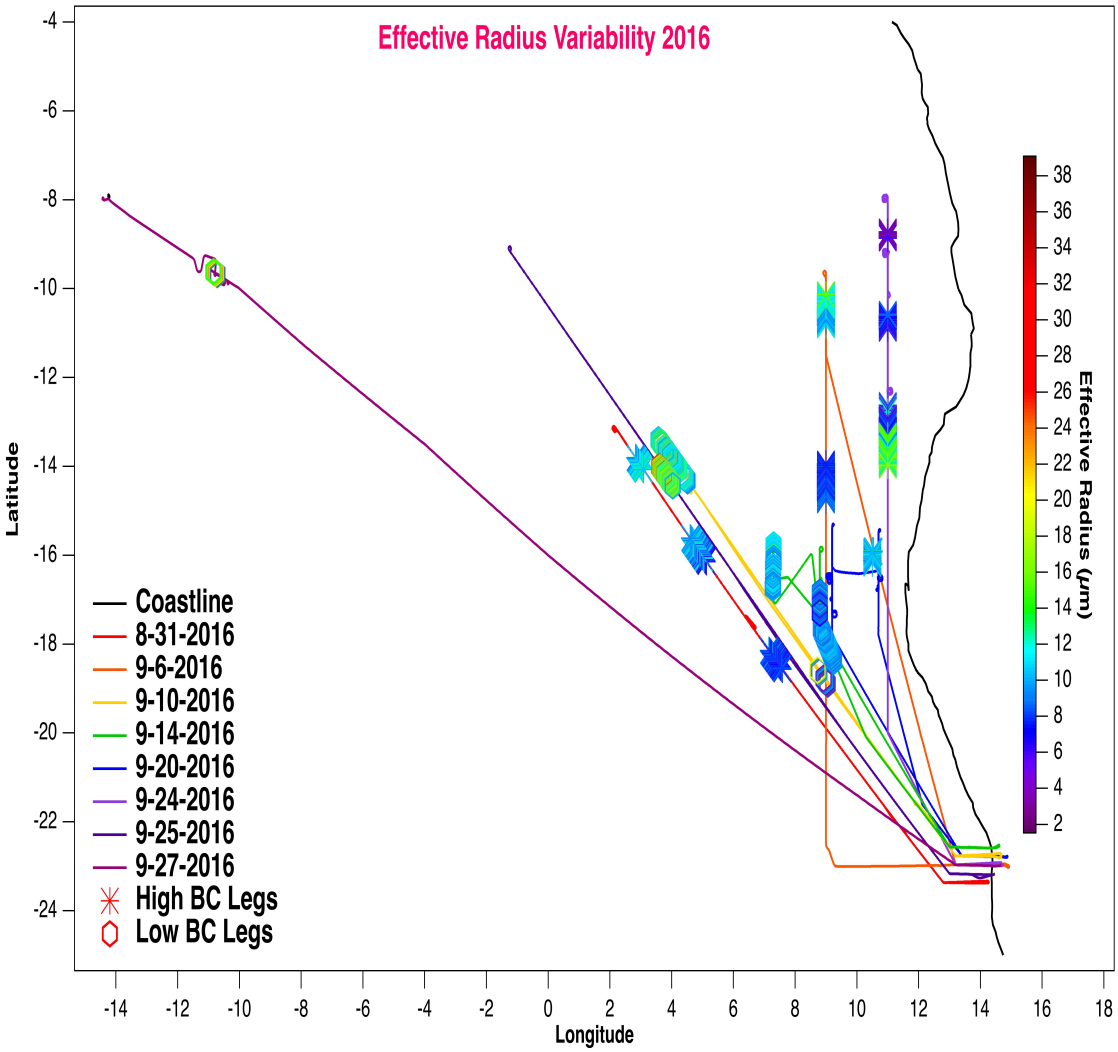

Figure 28 gives the variability of effective radius during the 2016 level legs with latitude on the left and longitude on the bottom. The west coast of Africa can be seen by the solid black contour. Only the high BC (>30 μg/m^3) and low BC (<2 μg/m^3) threshold legs are shown The flight paths are color-coded by flight date. High BC legs are shown as asterisks, and low BC legs are shown as hexagons.

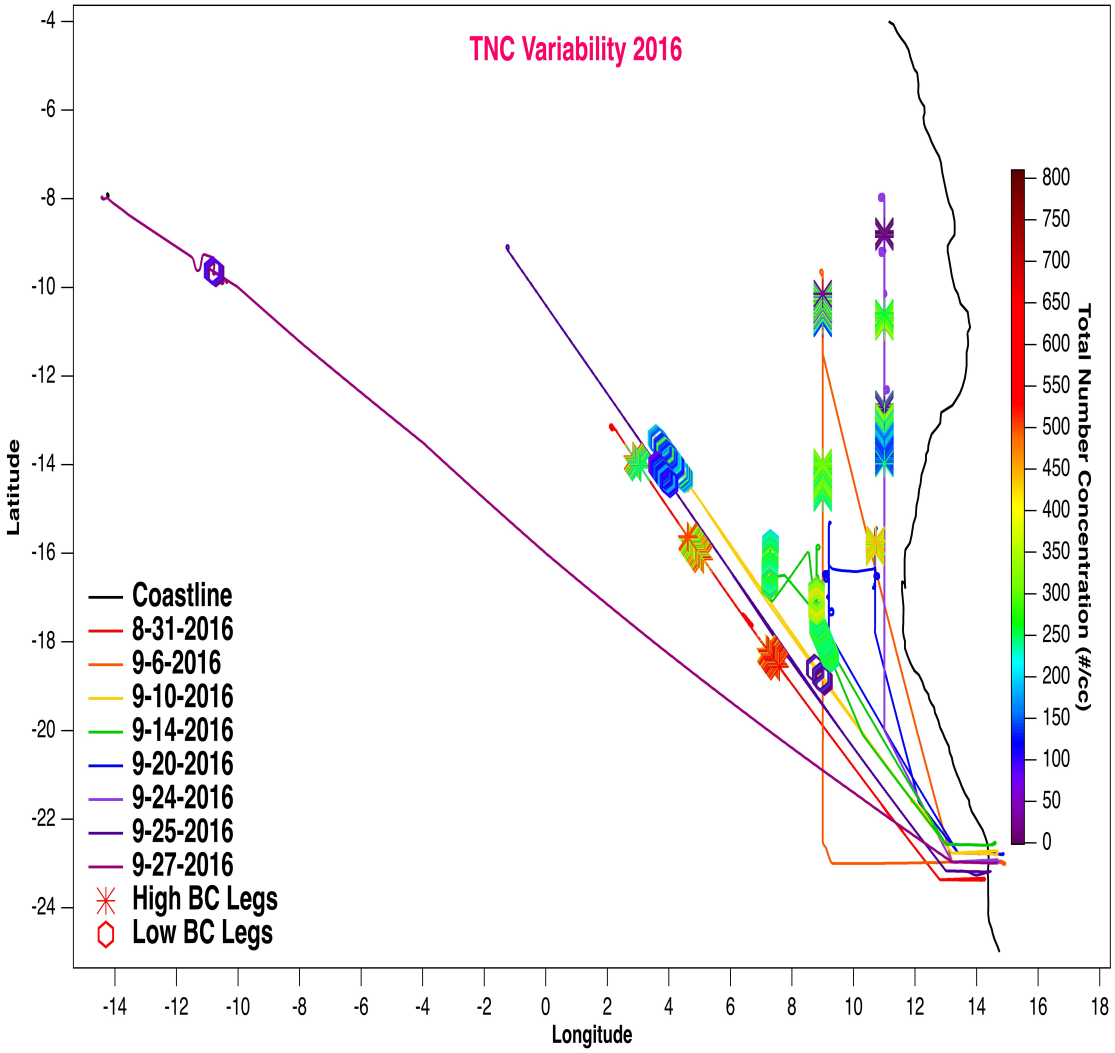

Figure 29 gives the variability of TNC during the 2016 level legs with latitude on the left and longitude on the bottom. The west coast of Africa can be seen by the solid black contour. Only the high BC (>30 μg/m^3) and low BC (<2 μg/m^3) threshold legs are shown The flight paths are color-coded by flight date. High BC legs are shown as asterisks, and low BC legs are shown as hexagons.

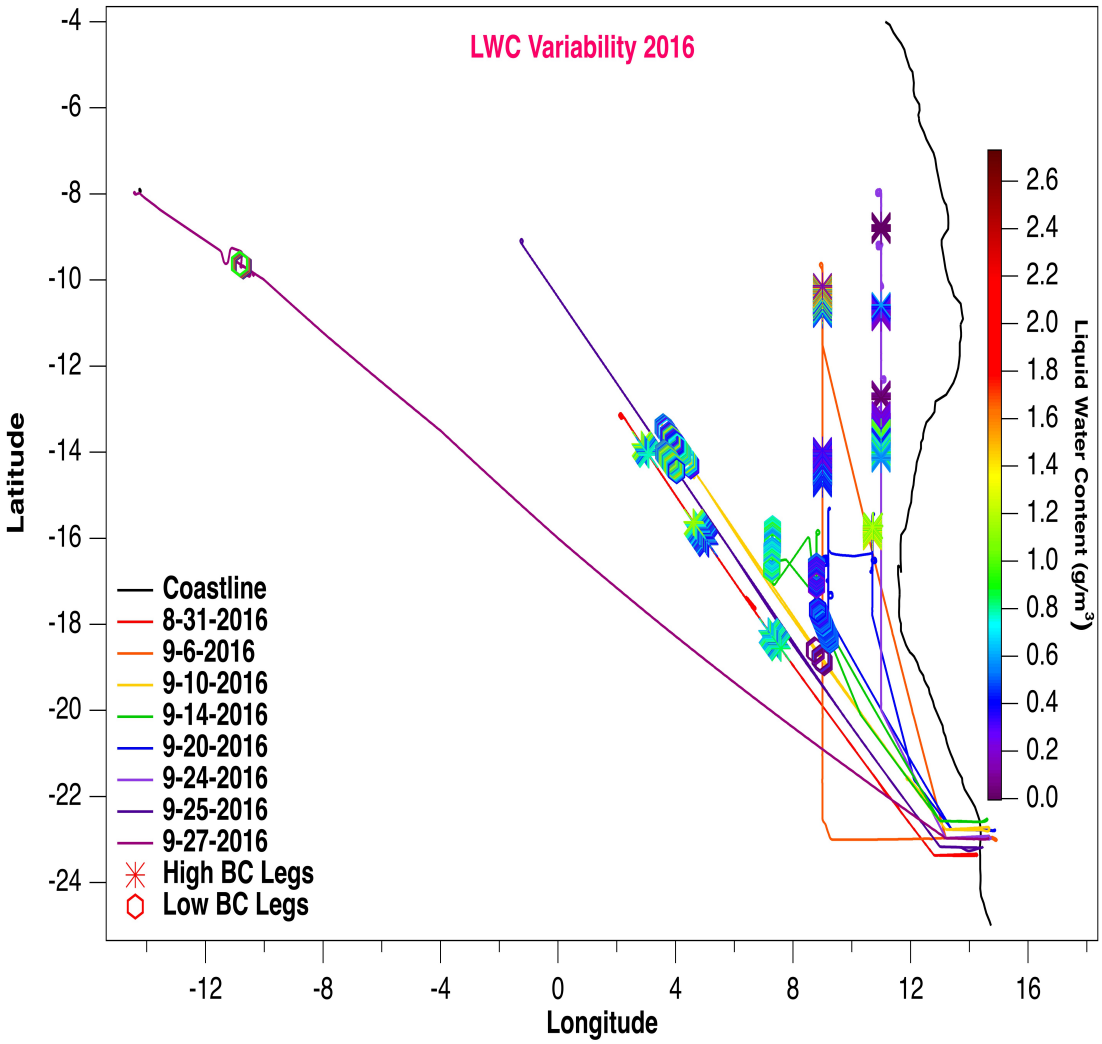

Figure 30 gives the variability of LWC during the 2016 level legs with latitude on the left and longitude on the bottom. The west coast of Africa can be seen by the solid black contour. Only the high BC (>30 μg/m^3) and low BC (<2 μg/m^3) threshold legs are shown The flight paths are color-coded by flight date. High BC legs are shown as asterisks, and low BC legs are shown as hexagons.

References

Ackerman, A. S., Kirkpatrick, M. P., 2004: The impact of humidity above stratiform clouds on indirect aerosol climate forcing. *Nature*., 432, 1014.

Adams, A.M., J.M. Prospero, and C. Zhang, 2012: CALIPSO-Derived Three-Dimensional Structure of Aerosol over the Atlantic Basin and Adjacent Continents. *J. Climate*, 25, 6862–6879.

Albrecht, B. A., 1989: Aerosols, cloud microphysics, and fractional cloudiness. *Science*, 245, 1227–1230.

Albrecht, B. A., M. P. Jensen, and W. J. Syrett, 1995b: Marine boundary layer structure and fractional cloudiness. *J. Geophys. Res.*, 100, 209–214.

Andreae, M. O., 1991: *Biomass Burning : Its history, use and distribution and its impact on the environmental quality and global climate, in: Global Biomass Burning: Atmospheric, Climatic and Bio-spheric Implications*, MIT Press, 3–21.

Angevine, W. M., J. E. Hare, C. W. Fairall, D. E. Wolfe, R. J. Hill, W. A. Brewer, and A. B. White, 2006: Structure and formation of the highly stable marine boundary layer over the Gulf of Maine. *J. Geophys. Res.*, 111.

Bretherton, C. S., J. Uchida, and P. Blossey, 2010b: Slow manifolds and multiple equilibria in stratocumulus-capped boundary layers. *J. Adv. Model. Earth Syst.*, 2.

Caldwell, P. and C.S. Bretherton, 2009: Response of a Subtropical Stratocumulus-Capped Mixed Layer to Climate and Aerosol Changes. *J. Climate,* 22, 20–38.

Chand, D., R. Wood, T. L. Anderson, S. K. Satheesh, and R. J. Charlson. 2009: Satellite-derived direct radiative effect of aerosols dependent on cloud cover, *Nat. Geosci*., 2, 181-184.

Chuang, P. Y., Saw, E. W., Small, J. D., Shaw ,R. A., Sipperly, C. M., Payne, G. A., and Bachalo , W. D., 2008: Airborne Phase Doppler Interferometry for Cloud Microphysical Measurements, *J. Aerosol Sci. and Tech.*, 42:8, 685-703.

Cotton, W.R. and Anthes, R.A., 1989: *Storms and Cloud Dynamics*. Academic Press, 883.

Duncan, B. N., R. V. Martin, A. C. Staudt, R. Yevich, and J. A. Logan., 2003: Interannual and seasonal variability of biomass burning emissions constrained by satellite observations, *J. Geophys. Res.*,108(D2), 4040.

Eastman, R., R. Wood, and K. T. O, 2017: The subtropical stratocumulus-topped planetary boundary layer: a climatology and the Lagrangian evolution. *J. Atmos. Sci.*, 74, 2633-2656.

Garay, M. J., S. P. de Szoeke, and C. M. Moroney, 2008: Comparison of marine stratocumulus cloud top heights in the southeastern Pacific retrieved from satellites with coincident ship-based observations. *J. Geophys. Res.*, 113, D18204.

Garratt, J. R., 1990: The internal boundary layer—A review. *Bound. Layer Meteor.*, 50, 171–203.

Garratt, J. R., 1992: *The Atmospheric Boundary Layer*. 1st ed. Cambridge University Press, 316.

Garreaud, R. D., J. Rutllant, J. Quintana, J. Carrasco, and P. Minnis., 2001: CIMAR-5: A snapshot of the lower troposphere over the subtropical southeast Pacific. *Bull. Amer. Meteor. Soc.*, 82, 2193–2207.

George, R. C., and R. Wood, 2010: Subseasonal variability of low cloud properties over the southeast Pacific Ocean. *Atmos. Chem. Phys.*, 10, 4047–4063.

Giglio, L., van der Werf, G. R., Randerson, J. T., Collatz, G. J., and Kasibhatla, P., 2006: Global estimation of burned area using MODIS active fire observations, *Atmos. Chem. Phys.*, 6, 957-974.

Hahn, C.J., and S.G. Warren, 2007: A gridded climatology of clouds over land (1971-96) and ocean (1954-97) from surface observations worldwide. Report NDP-026E, 71.

Hansen, J., Sato, M., and Ruedy, R., 1997: Radiative forcing and climate response, *J. Geophys. Res.*, 102, 6831–6864.

Hartmann, D., M. Ockert-Bell, and M. Michelsen, 1992: The effect of cloud type on Earth's energy balance: Global analysis. *J. Climate*, 5, 1281-1304.

Houze, R., 2014: *Cloud Dynamics*. 2nd ed., Elsevier B.V., 496.

Huang, J., T. Wang, W. Wang, Z. Li, and H. Yan (2014), Climate effects of dust aerosols over East Asian arid and semiarid regions, *J. Geophys. Res. Atmos.*, 119, 11,398–11,416.

Hudson, J.G. and S.S. Yum, 1997: Droplet Spectral Broadening in Marine Stratus. *J. Atmos. Sci.* 54, 2642–2654.

Jiang, H., G. Feingold, and W. R. Cotton., 2002: Simulations of aerosol-cloud-dynamical feedbacks resulting from entrainment of aerosol into the marine boundary layer during the Atlantic Stratocumulus Transition Experiment, *J. Geophys. Res.*, 107, 4813.

Johnson, B. T., K. P. Shine, and P. M. Foster, 2004: The semi-direct aerosol effect: Impact of absorbing aerosols on marine stratocumulus, *Q. J. R. Meteorol. Soc.,* 130, 1407-1422.

Klein, S. A., D. L. Hartmann, and J. R. Norris, 1995: On the relationships among low-cloud structure, sea surface temperature, and atmospheric circulation in the summertime northeast Pacific. *J. Climate*, 8, 1140–1155.

Klein, S. A., 1997: Synoptic variability of low-cloud properties and meteorological parameters in the subtropical trade wind boundary layer. *J. Climate*, 10, 2018–2039.

Kloesel, K.A., 1992: A 70-Year History of Marine Stratocumulus Cloud Field Experiments off the Coast of California. *Bull. Amer. Meteor. Soc.,* 73, 1581–1586.

Lohmann, U., and J. Feichter, 2005: Global indirect aerosol effects: A review. *Atmos. Chem. Phys.*, 5, 715–737.

Lilly, D. K., 1968: Models of cloud-topped mixed layers under a strong inversion. *Quart. J. Roy. Meteor. Soc.*, 94, 292–309.

Liu, Yongqiang; Goodrick, Scott; Heilman, Warren. 2014. Wildland fire emissions, carbon, and climate: Wildfire–climate interactions. *Forest Ecology and Management*. 317: 80-96.

Lu, M.-L., W. C. Conant, H. H. Jonsson, V. Varutbangkul, R. C. Flagan, and J. H. Seinfeld., 2007: The Marine Stratus/Stratocumulus Experiment

(MASE): Aerosol-cloud relationships in marine stratocumulus, *J. Geophys. Res.*, 112.

Lu, M.-L., A. Sorooshian, H. H. Jonsson, G. Feingold, R. C. Flagan, and J. H. Seinfeld., 2009: Marine stratocumulus aerosol-cloud relationships in the MASE-II experiment: Precipitation susceptibility in eastern Pacific marine stratocumulus, *J. Geophys. Res.*, 114.

Matichuk, R. I., P. R. Colarco, J. A. Smith, and O. B. Toon. 2007: Modeling the transport and optical properties of smoke aerosols from African savanna fires during the Southern African Regional Science Initiative campaign (SAFARI 2000), *J. Geophys*. Res., 112.

Miles, N.L., J. Verlinde, and E.E. Clothiaux, 2000: Cloud Droplet Size Distributions in Low-Level Stratiform Clouds. *J. Atmos. Sci.,* 57, 295–311.

Morgan, M. G., P. J. Adams, and D. W. Keith., 2006: Elicitation of expert judgements of aerosol forcing, *Clim. Change,* 75, 195-214.

Muhlbauer, A., and McCoy, I. L., and Wood, R., 2014: Climatology of stratocumulus cloud morphologies: microphysical properties and radiative effects. *Atmos. Chem. Phys*., 14, 6695-6716.

Paluch, I.R. and D.H. Lenschow, 1991: Stratiform Cloud Formation in the Marine Boundary Layer. *J. Atmos. Sci.,* 48, 2141–2158.

Painemal, D., S. Kato, and P. Minnis., 2014: Boundary layer regulation in the southeast Atlantic cloud microphysics during the biomass burning season as seen by the A-train satellite constellation. *J. Geophys. Res.*, 119, 11,288–11,302.

Penner, J. E., and Quaas, J., and Storelvmo, T., et al., 2006: Model intercomparison of indirect aerosol effects. *Atmos. Chem. Phys*., 6, 3391-3405.

Ramanathan, V., Carmichael, G., 2008: Global and regional climate changes due to black carbon. *Nature Geosci*., 1, 221-227.

Reid, J.S., Hobbs, P.V., Rangno, A.L., and Hegg, D.A., 1999: Relationship between cloud drop effective radius, liquid water content, and droplet concentration for warm clouds in Brazil embedded in biomass smoke. *J. Geophys. Res.*., 104, 6145-6153.

Roberts, G., and Wooster, M. J., and Lagoudakis, E., 2009: Annual and diurnal African biomass burning temporal dynamics. *Biogeosciences*., 6, 849-866.

Rosenfeld, D., 1999: TRMM observed first direct evidence of smoke from forest fires inhibiting rainfall, *Geophys. Res. Lett.,* 26, 3105-3108.

Sakaeda, N., R. Wood, and P. J. Rasch., 2011: Direct and semidirect aerosol effects of southern African biomass burning aerosol, *J. Geophys. Res.*, 116.

Schulz, M., Schulz, M., Textor, C., Kinne, S., Balkanski, Y., Bauer, S., Berntsen, T., Berglen, T., Boucher, O., Dentener, F., Guibert, S., Isaksen, I. S. A., Iversen, T., Koch, D., Kirkev, A., Liu, X., Montanaro, V., Myhre, G., Penner, J. E., Pitari, G., Reddy, S., Seland., Stier, P. and Takemura, T.2006: Radiative forcing by aerosols as derived from the AeroCom present-day and pre-industrial simulations, *Atmos. Chem. Phys*., 6, 5225-5246.

Schwarz, J. P., R. S. Gao., D. W. Fahey., D. S. Thomson., L. A. Watts., J. C. Wilson., J. M. Reeves., M. Darbeheshti., D. G. Baumgardner., G. L. Kok., S. H. Chung., M. Schulz., J. Hendricks., A. Lauer., B. Kärcher., J. G. Slowik., K. H. Rosenlof., T. L. Thompson., A. O. Langford., M. Loewenstein., K. C. Aikin., 2006: Single-particle measurements of midlatitude black carbon and light-scattering aerosols from the boundary layer to the lower stratosphere, *J. Geophys. Res.*, 111.

Sporre, M. K., Swietlicki, E., Glantz, P., and Kulmala, M., 2014: Aerosol indirect effects on continental low-level clouds over Sweden and Finland, *Atmos. Chem. Phys*., 14, 12167-12179.

Stephens, G.L., and Greenwald, T.J., 1991: The Earth's radiation budget and its relation to atmospheric hydrology: 2. Observations of cloud effects. *J. Geophys. Res*., 96, 15325-15340.

Swap, R. J., and Privette, J. L., 1999: Overview of the Southern African Regional Science Initiative-SAFARI 2000., International Geoscience and Remote Sensing Symposium., 1, 595-597.

Thompson, W. T., S. D. Burk, and J. Lewis, 2005: Fog and low clouds in a coastally trapped disturbance. *J. Geophys. Res.*, 110**.**

Toniazzo, T., S. J. Abel, R. Wood, C. R. Mechoso, G. Allen, and L. C. Shaffrey, 2011: Large-scale and synoptic meteorology in the south-east

Pacific during the observations campaign VOCALS-REx in austral Spring 2008. *Atmos. Chem. Phys.*, 11, 4977–5009.

Twohy, C. H., and Anderson, J. R., 2008: Droplet nuclei in non-precipitating clouds: composition and size matter. *Envir. Res. Lett*., 3, 45002.

Twomey, S., 1974: Pollution and the planetary albedo. *Atmospheric Environment*., 8, 1251-1256.

Twomey, S., 1977: The influence of pollution on the shortwave albedo of clouds. *J. Atmos. Sci.*, 34,1149–1152.

Van der Werf, G. R., Randerson Collatz, G. J., and Giglio, L., 2003: Carbon emission from fires in tropical and subtropical ecosystems, *Glob. Change Biol*., 9, 547–562,.

Van der Werf, G. R., Randerson, J. T., Giglio, L., Collatz, G. J., Kasibhatla, P. S., and Arellano Jr., A. F., 2006: Interannual variability in global biomass burning emissions from 1997 to 2004, *Atmos. Chem. Phys*., 6, 3423–3441.

Wallace, J., and Hobbs, P., 2006: *Atmospheric Science*. 2nd ed., Elsevier B.V., 504.

Warren, S. G., C. J. Hahn, J. London, R. M. Chervin, and R.L. Jenne, 1986: Global distribution of total cloud cover and cloud type amounts over land. NCAR Tech. Note TN-273 + STR, 229.

Warren, S. G., C. J. Hahn, J. London, R. M. Chervin, and R.L. Jenne, 1988: Global distribution of total cloud cover and cloud type amounts over the ocean. NCAR Tech. Note TN-317 + STR, 212.

Wood, R., and C. S. Bretherton, 2004: Boundary layer depth, entrainment, and decoupling in the cloud-capped subtropical and tropical marine boundary layer. *J. Climate*, 17, 3576–3588.

Wood, R., 2006: Rate of loss of cloud droplets by coalescence in warm clouds, *J. Geophys. Res.*, 111.

Wood, R., and D. L. Hartmann, 2006: Spatial variability of liquid water path in marine boundary layer clouds: The importance of mesoscale cellular convection. *J. Climate*, 19, 1748–1764.

Wood, R., 2007: Cancellation of Aerosol Indirect Effects in Marine Stratocumulus through Cloud Thinning. *J. Atmos. Sci.,* 64, 2657–2669.

Wood, R., 2012: Stratocumulus Clouds. *Mon. Wea. Rev*., 140, 2373-2423.

Young, K. C., 1993: *Microphysical Processes in Clouds*. Oxford University Press, 427.

Zhu, P., Zhu, P., C.S. Bretherton, M. Köhler, A. Cheng, A. Chlond, Q. Geng, P. Austin, J. Golaz, G. Lenderink, A. Lock, and B.
Stevens., 2005: Intercomparison and interpretation of single-column model simulations of a nocturnal stratocumulus-topped marine boundary layer. *Mon. Wea. Rev*., 133, 2741–2758.